공학박사학위논문

형상기억 합금을 이용한 마이크로스케일 고속 구동기의 제작 및 평가

Design, Fabrication and Evaluation of High Speed Microscale Shape Memory Alloy Actuator

2017년 8월

서울대학교 대학원

기계항공공학부

이 현 택

Abstract

Design, Fabrication and Evaluation of High Speed Microscale Shape Memory Alloy Actuator

Hyun-Taek Lee

Department of Mechanical and Aerospace Engineering

The Graduate School

Seoul National University

We designed, fabricated, and evaluated a shape memory alloy-based microscale actuator. To achieve complex shape fabrication and an in situ mechanical characterization, a manipulation and characterization platform equipped with high-resolution nanopositioners (with multiple degrees of freedom) and a micro-force sensor was developed. The challenges inherent in precise and accurate fabrication of samples with complex geometry were overcome so that the platform can be used for mechanical property characterization with an in situ method in the high vacuum chamber of a focused ion beam (FIB) system.

Using the developed platform, diamond-shaped frame structures 1–1.5 μm in thickness were manufactured using an FIB milling process with a shape memory alloy (SMA). The behavior of these structures under mechanical deformation and changes in thermal conditions was investigated with respect to use as a driving force for a high-speed microscale actuator. Thermal energy was delivered by an optical method, including ion beam irradiation and laser irradiation. Because this method does not require any wiring, unlike other heating methods such as Joule heating, we could realize the fabricated SMA structure without any structural interruptions that could negatively affect the fast actuation motion.

As an application, a microscale actuator is proposed. Due to the scale effect, a microscale linear motion actuator can vibrate at over 500 Hz with laser-induced heating. The reaction force and response speed were investigated according to changes in the laser switching speed and power. Additionally, a gripper having a negative Poisson's ratio structure could grab small objects and deliver an objective by triggering the shape memory effect. We expect the proposed actuators to contribute to the development of micro- and nanoscale devices for microscale investigations and medical purposes.

Keywords: Shape memory alloy, Micro actuator, Focused Ion Beam, In-situ manipulation

Student Number: 2011-23340

Contents

List of Figures

List of Tables

Chapter 1. Introduction

1.1. Toward miniaturization

In the last decades, researches on developing microscale actuators were studied and various design in microscale structures was proposed. Researchers are expecting that these robots can be used for biomedical purposes such as drug delivery or tissue engineering. Various kind of driving forces such as magnetic, thermal, electrostatic was used. Among them, almost every micro-robots adopts magnetic force as a driving source.

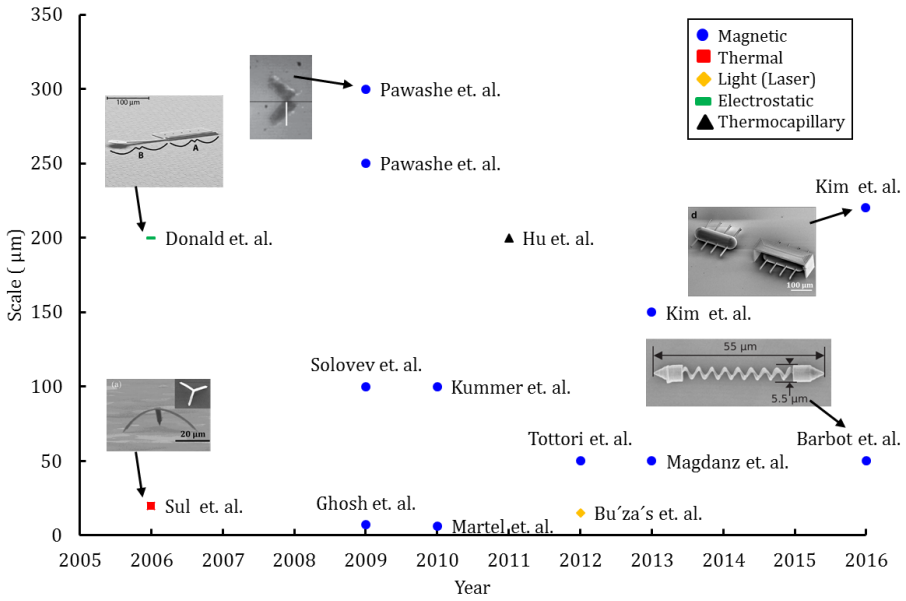

Figure 1 Recent research for developing microscale robots [1-18]

When we see more details of current research, we can aware that recently developed micro-robots use two-photon lithography as a manufacturing method. This manufacturing process is available to build full 3D structure and it is good to the mass production due to the relatively easy manufacturing process. However, because the structures consist of crystallized polymers so it cannot deform the shape and even does not respond at magnetic field. All of the structures were coated by nickel of other metals to drive by magnetic force. These robots were dragged or shaken by the change of magnetic field to generate thrust force. However, because it cannot deform structure, these robots have a limitation in manipulating targets.

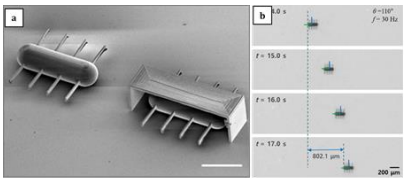

Magnetically actuated ciliary microrobots (Kim et. al. , 2016)

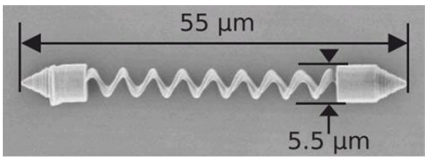

Magnetic Microfluidic Multimodal Swimmer (Barbot et. al., 2016)

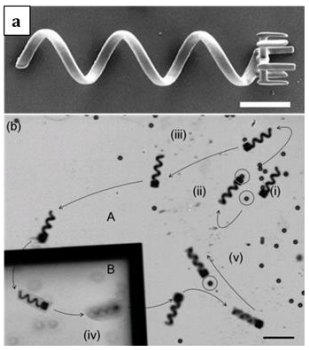

Magnetic Helical Micromachine (Tottori et. al., 2012)

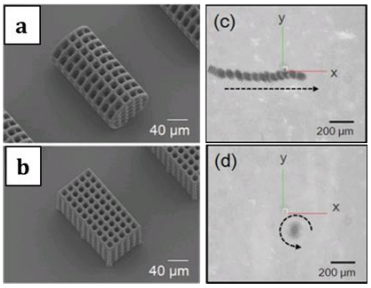

Magnetic microrobots for Cell Culture (Kim et. al. , 2013)

Figure 2 Recent developed microscale robots

1.2. Shape Memory Alloy (SMA)

In terms of a driving source for the microactuator, shape memory alloy called as SMA is one of the best candidates. SMAs are the unique material, which “remember” their original shapes. SMA can be made with a various components such as Fe-Mn-Si, Cu-Zn-Al, Cu-Al-Ni, and Ni-Ti. Among them, Ni-Ni, named as Nitinol, is considered a breakthrough for engineering applications and this alloy shows superior characteristic in terms of shape memory effect (SME) among all SMAs [19]. Nitinol possesses two different crystal structure called martensite and austenite and the phase depends on the temperature (Figure 3). The material properties of NiTi are summarized in Table 1 [19].

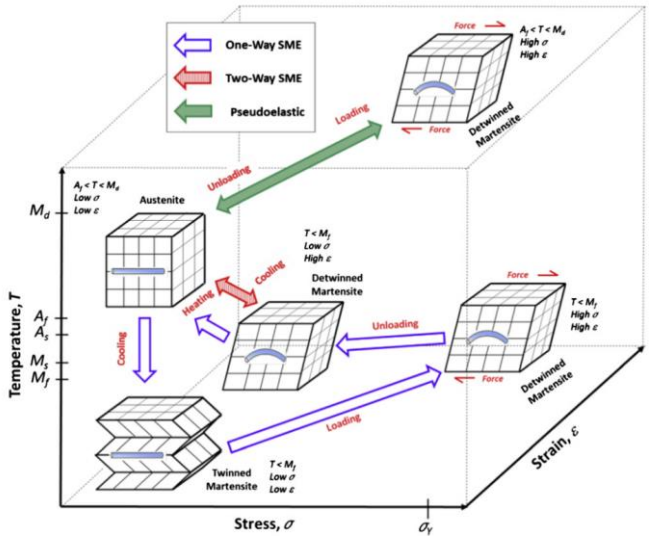

Figure 3 schematic diagram of SMA phases and crystal structures [20]

Table 1 Material Properties of NiTi SMA [19, 21, 22]

Properties	Value
Melting Point	1240 – 1310 ℃
Density	6.4 – 6.5 g/cm^3
Thermal Conductivity (austenite)	18 W/m·K
Thermal Conductivity (martensite)	8.6 W/m·K
Specific Heat	470 – 620 J/kg·K
Latent Heat	24,200 J/kg
Transformation Range	−200 – 110 ℃
Transformation Hysteresis	30 – 50 ℃
Yield Strength (austenite)	200 – 800 MPa
Young's Modulus (austenite)	50 – 90 GPa
Yield strength (martensite)	150 – 300 MPa
Young's Modulus (martensite)	28 – 41 GPa
Ultimate Tensile Strength	750 – 960 MPa
Shape Memory Strain (max.)	~8.0%
Resistivity (austenite)	70 – 110 μΩcm
Resistivity (martensite)	40 – 70 μΩcm

1.3. Shape memory alloy based microscale actuator

Micro-actuation is researched widely for developing an application for various purposes such as biomedical devices, microsensors, microfluidics area. Many types of smart materials including a piezoelectric material, shape memory alloy, magnetic materials are used for actuation source. Among them, shape memory alloy (SMA) is one of the promising candidates and studied widely because it can generate significant force and displacement (work density) compared to other actuation sources [20]. Even more, SMA has a unique property such as shape memory effect (SME), superelasticity (pseudoelasticity) and high power to weight ratio and good biocompatibility [19, 23]. In terms of making micro-/nanoscale actuation, SMA is promising actuation source because shape memory effect is maintained even in tens of nanometer scale [24, 25]. Including shape memory effect, various types of physics such as electrostatic, electromagnetic or piezoelectric were adopted for microscale actuation. Among them, shape memory alloy possesses uniquely high work density than other methods, so it can give much actuation force than other sources. However, relatively slow actuation speed is a limitation of shape memory alloy. To utilize SMA more efficiently, we need to develop high-frequency actuation method.

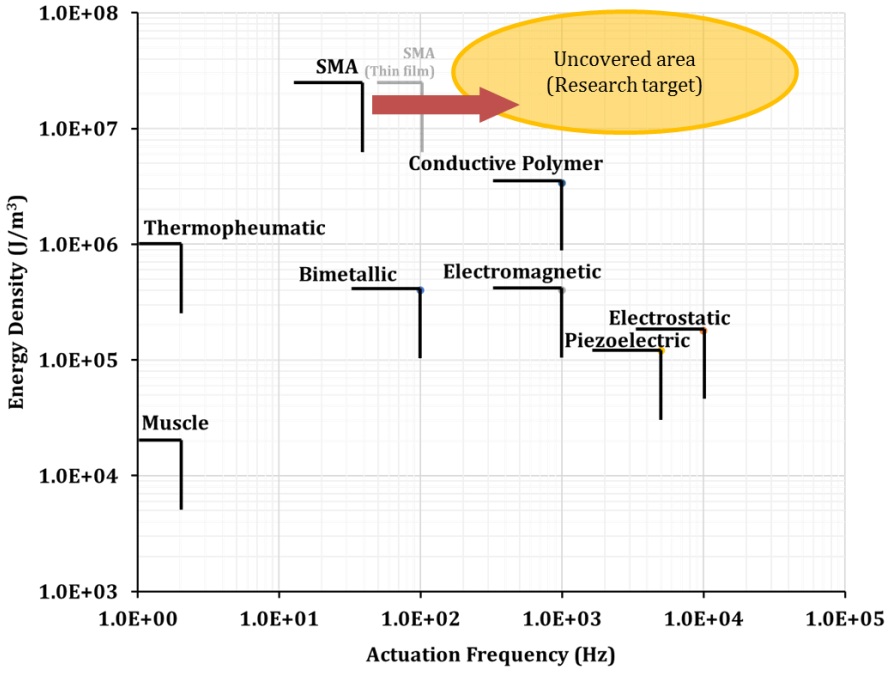

Figure 4 Various types of driving forces for microscale actuation

1.4. Focused Ion Beam technique in micro- and nanoscale structuring

As described in Figure 5, FIB processing can be categorized as four, 1) milling (sputtering and etching), 2) deposition, 3) implantation, and 4) imaging [26]. Among them, milling and deposition method are related to direct structure fabrication. The implantation can modify chemical or mechanical properties of the surface of the target material. The imaging is used for micro/nano-analysis.

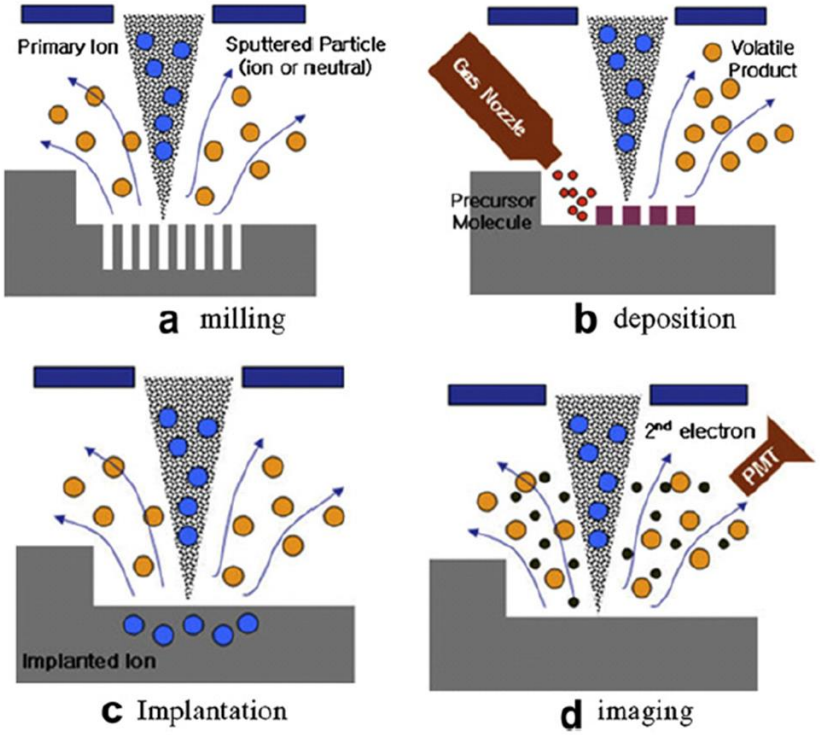

Figure 5 Schematic diagram of FIB processes

a) milling, 2) deposition, 3) implantation, and 4) imaging [26]

Focused ion beam (FIB) milling technique is one of the strong tools for micro-/nanoscale fabrication process because it can fabricate a structure on solid without any mask or post processing regardless of the type of material within tens of nanometer resolution. With these advantages, FIB technique is widely used in micro-/nanoscale fabrication. Figure 6 shows some examples of microscale features fabricated by focused ion beam milling [27] and Figure 7 shows those of made by deposition method [28].

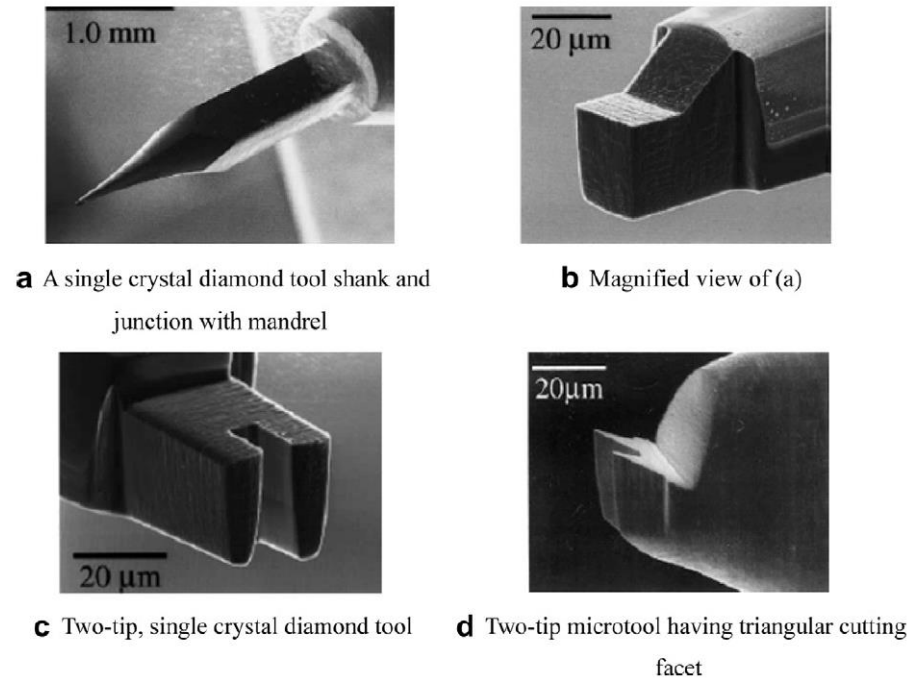

a A single crystal diamond tool shank and junction with mandrel

b Magnified view of (a)

c Two-tip, single crystal diamond tool

d Two-tip microtool having triangular cutting facet

Figure 6 Mechanical cutting tools fabricated by FIB milling process [27]

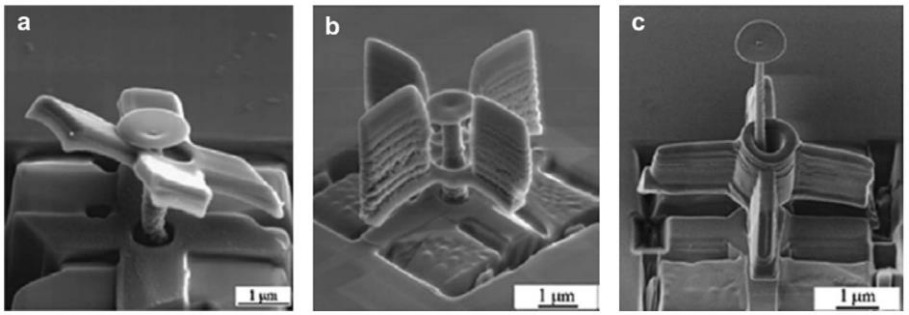

Figure 7 Microscale windmill fabricated by FIB deposition process [28]

1.5. In-situ characterization in SEM/FIB system

There have been significant advances in real-time imaging and sample preparation techniques over the past few decades. In-situ characterization/modification methods [29-35], for example, scanning electron microscopy (SEM), focused ion beam (FIB) and FIB-SEM dual beams, use nanomanipulators with mechanical, electrical, and/or thermal measurement probe attachments. The main advantage of this kind of in-situ characterization is that the measurement process can be operated under real-time observation; thus, it is highly reliable. There are various techniques to study mechanics on very small scales, such as tension, compression, bending, torsional and nanoindentation tests [33, 36-38]. These methods are frequently combined with electron microscopy to take advantage of in-situ measurement techniques [34]. Many researchers have investigated the micromechanical properties of biological materials using FIB milling and micro-characterization systems [39, 40]. FIB systems equipped with a variety of sensors have proven to be reliable with respect to their ability to resolve localized features at micro- and nanoscales. The most interesting feature of FIB technology is the localized sample preparation method, which uses a milling process. Using FIB milling, it is possible to fabricate a sample directly without the need for post-processing. The milling process can be used on almost any type of material and is not limited by the shape of the sample [26, 41]. However, it can be

difficult to measure the mechanical properties of samples with intricate geometries. This is because the FIB sample preparation and handling process has limitations when extracting samples from specific locations and requires delicate, complicated procedures. Adineh et al. [42] characterized biomechanical structures in rat whiskers using FIB combined with atomic force microscopy (AFM). A micro-gripper system was used to overcome difficulties in controlling the sample whilst it is attached to the substrate. Some disadvantages, such as desiccation, arise from the use of a vacuum environment [43, 44]. Whereas the nanoindentation technique, for characterizing hardness, elasticity or fracture, can be applied to a wetted sample or in a humidified chamber, measurements in this equipment are constrained by having to use a matrix to hold the material. This can introduce variability and errors. The FIB platform approach is superior in that it avoids the need for a matrix, but it is limited to dry samples unless a specialized cold stage is used that allows samples to be 'wet'. So, if used under full vacuum conditions the FIB platform should be seen as complementary to current approaches rather than a replacement technique.

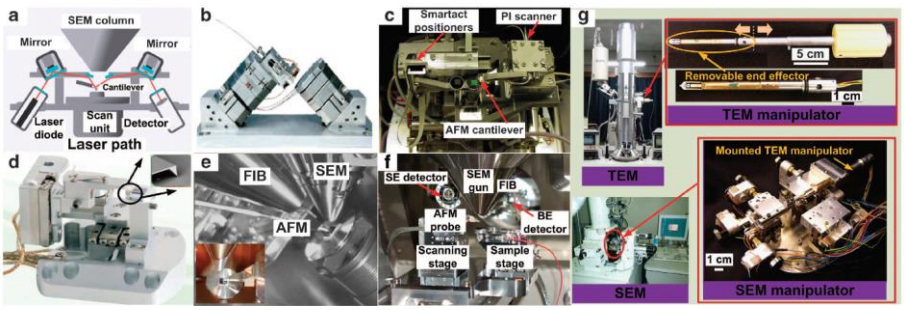

Figure 8 Examples of manipulation/evaluation platforms in the SEM/FIB platform [45]

1.6. Goals of this research

In this study, a sample manipulation and evaluation platform operate in FIB system will be proposed and developed. With this proposed platform, various type of specimens which require complicate sample manipulation process or micromechanical characterization will be fabricated and evaluated as case studies of usage of the platform. As a novel application for developing microscale actuator fabricated with this platform, a simple actuation device consists of shape memory alloy were fabricated by the focused ion beam milling process.

At the structure, mechanical behavior under deformation and appearance of shape memory effect by ion beam induced heating method will be investigated through in-situ method. In addition, to investigate feasibility on actuation under ambient condition, laser induced heating test was conducted. The actuation responses regarding laser power and frequency variation will be observed to utilize shape memory effect for microscale actuation. Based on these test results, shape memory alloy based microscale applications such as the micro-gripper and high-frequency linear actuator will be proposed and fabricated.

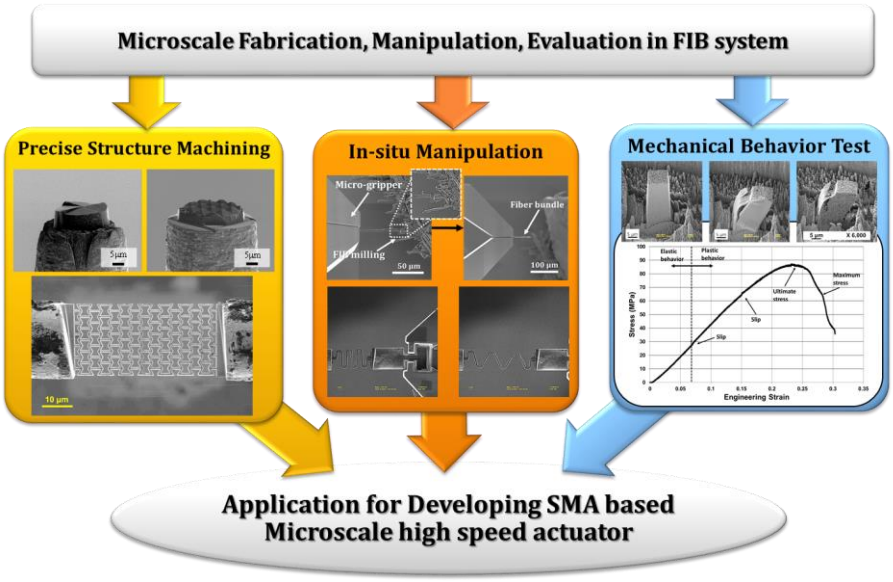

Figure 9 Goal of this research

Chapter 2. Platform for manufacturing and test

2.1. Focused Ion Beam (FIB) system

All procedures regarding sample fabrication and mechanical property test were conducted in in-situ nanomanipulation platform attached ion FIB vacuum chamber. Two nanopositioners equipping jig for micro-SMA wire and microforce sensor were installed inside the FIB chamber. Figure 10 is a picture of focused ion beam system used for this experiment. At the custom manufactured chamber, FIB column (COBRA, Orscyphysics, France), high precision 5-axis eucentric stage (UST-5100, FJELD, U.S.A.) and vacuum systems were installed.

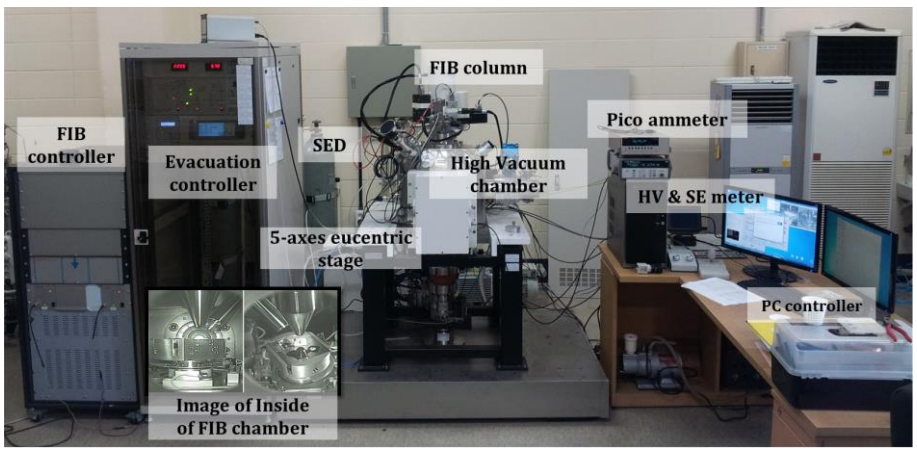

Figure 10 Picture of focused ion beam (FIB) system

2.2. Platform design of in-situ fabrication and evaluation

To utilize sample manipulation/test platform in FIB system, A 4-axis (X, Y, Z and R axis) nano-positioner and a 3-axis (X, Y, Z axis) are used to achieve precise positioning and degree of freedom in sample manipulation. In addition, micro-grippers (FT-G102, FemtoTools, Germany), micro-force sensors (FT-S1000, FemtoTools, Germany) or sample fixtures can be mounted at the end of the nanopositioners as an end-effector. These nanopositioners equipping end-effectors can be mounted on the customized base plates according to the purpose of the experiment and installed in 5-axis eucentric FIB stage. Those mounts, nanopositioners, and end-effectors can be chosen among in several modules according to the experimental purpose or sample geometry.

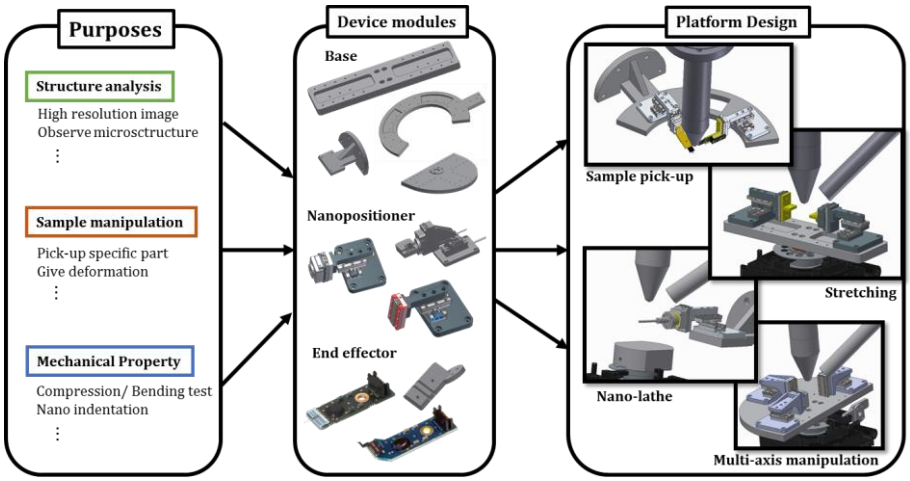

Figure 11 Concept for in-situ fabrication/evaluation platform in FIB system

2.3. Application of developed platform: Case studies

Case study 1: Complex geometry fabrication[1]

With the aid of manipulation platform, microstructures having complex geometry can be fabricated in a one-step procedure. As an example, microscale cutting tools with complex blade shapes were fabricated by developed manipulation platform. Figure 12 is the platform used for tool fabrication. Shaft shaped tungsten carbide

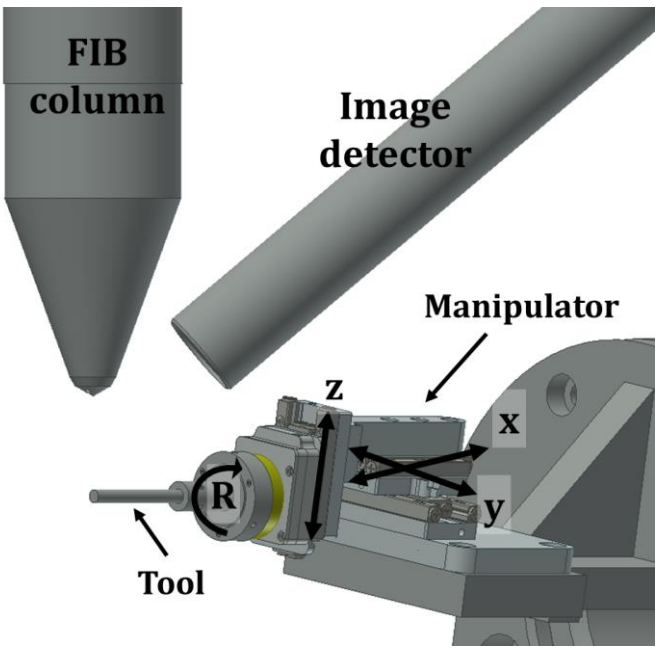

Figure 12 Conceptual design of in-situ manipulation platform for micro-lathe

[1] This part is published at the journal paper, Bilegt, E., et al., Design and evaluation of micro-cutting tools for local planarization. International Journal of Precision Engineering and Manufacturing, 2016. 17(10): p. 1267-1273.

The whole fabrication process for a multiple-lattice cutting-edge tool is described in Figure 13. FIB milling area and the observed from the other side were marked in the blue and red box respectively. For the FIB sputtering parameters, a 10 μs of dwell time and 50% beam overlap were used as common conditions. Various probe currents were used for each step. A 2,500-pA beam current was used to fabricate the rough milling processes and both 716-pA and 139-pA beam currents were used for the fine milling processes that require high accuracy, such as cutting-edge and clearance angle fabrication.

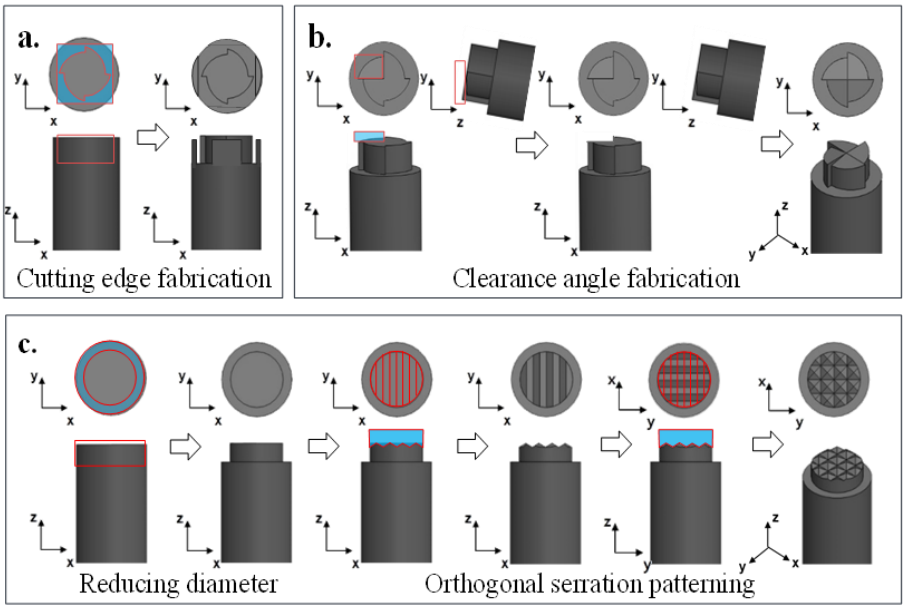

Figure 13 Fabrication procedure of 30-μm-diameter micro-cutting tools using FIB: (a) cutting-edge fabrication, (b) clearance-angle fabrication through rotation, and (c) multiple-lattice edge tool [46]

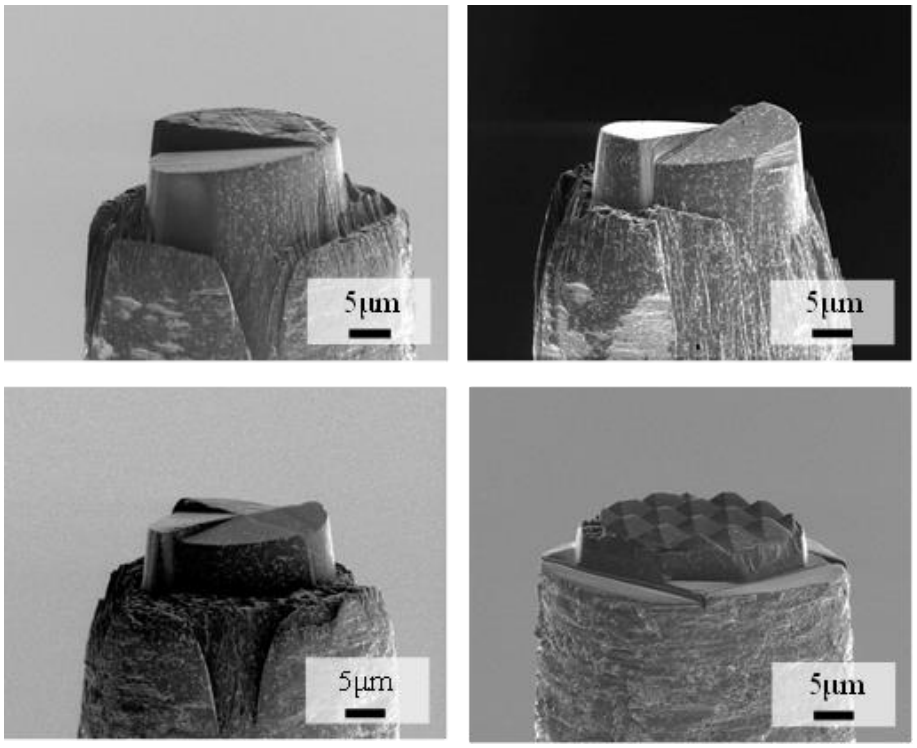

Figure 14 Micro-cutting tools fabricated with FIB [46]

Figure 14 is scanning electron microscope (SEM) images of fabricated micro-tool. As shown in these pictures, three-dimensional structures can be fabricated easily under this manipulation platform without sample transfer or re-attachment.

Case study 2: In-situ mechanical characterization[2]

Biological materials are the result of years of evolution and possess a number of efficient features and structures. Researchers have investigated

[2] This part is published at the paper Lee, H.-T., et al., Site-specific characterization of beetle horn shell with micromechanical bending test in focused ion beam system. Acta Biomaterialia, 2017

the possibility of designing biomedical structures that take advantage of these structural features. Insect shells, such as beetle shells, are among the most promising types of biological material for biomimetic development. As shown in Figure 15, the cross-sectional and transversal images show that both parts of the procuticle layer consist of a protein matrix and chitin fibers [47-49]. The layers frequently have different geometrical arrangements. The geometrical arrangements can vary due to the direction of lamination, the combination of chitin fibers, and the protein matrix. Due to their intricate geometries and small sizes, it is challenging to measure the mechanical properties of these microscale structures.

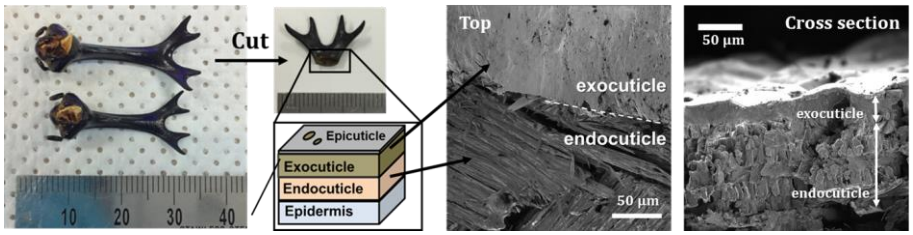

Figure 15 A picture of the beetle horn used for imaging and a schematic diagram of the layered composition of the shell

An in-situ testing platform for site-specific experiments in a focused ion beam (FIB) system is good tool to overcome this problem. Multi-axis nanomanipulators and a micro-force sensor were utilized in the testing

platform to allow better results in the sample preparation and data acquisition.

As mentioned, manipulating and characterizing microscale structures is a complicated process. When measuring biological materials, such as beetle shell, it can be difficult to determine an exact position due to the non-uniform shape and unpredictable composition of the material. This contrasts to the measurement of well-defined artificial materials. FIB has been used to prepare mechanical test specimens at micro- and nano-scale in last two decades [42, 50]. In our study, we used FIB to make the cantilevers of endocuticle and exocuticle to implement the micro-bending test. In the case of fiber bundle bending tests, however, extracting a single fiber bundle from the endocuticle layer is not possible using conventional FIB techniques. For this reason, we used a specialized gripping and detaching method to manipulate the extremely small samples with complex geometries in FIB. Figure 16 shows the conceptual design of the system developed for this purpose, and the resulting platform. To equip the in-situ testing system with sample manipulation abilities, a precise manipulation and sensing platform was devised. One 4-axis (X, Y, Z and R axis) nano-positioner and one 3-axis (X, Y and Z axis) nano-positioner (SLC-1730 for linear positioning and SR-2013-S for rotational positioning, respectively, SmarAct GmbH, Oldenburg, Germany) were mounted on the cradle of a 5-axes eucentric stage instead of mounting on chamber wall.

This enable us to manipulate the 4-axes and 3-axes nano-positioners on the basis of 5-axes eucentric stage. Thus, whole coordinate system moves simultaneously. The design supports the addition of a variety of end effectors to the end of the manipulator. Depending on the experiment, these might include force sensors, grippers, electric measuring probes and sample holders. These manipulators, as well as the eucentric stage, which has 12-degree of freedom in total, can be operated simultaneously inside the vacuum chamber. The positioning resolution is on the order of tens of nanometers. Thus, the end effectors can be positioned precisely.

For micromechanical characterization based on a bending test, a micro-force sensor end effector (FT-S10000; FemtoTools GmbH, Zurich, Switzerland) was mounted on the 3-axis nano-positioner. The sensor collected reaction force data with micronewton precision along the axis orthogonal to the sensor's probe axis. The original size of the sensor tip was 50 × 50 μm, but we redesigned it and created a custom-machined 10 × 10-μm square tip using FIB milling. The new tip was appropriate for the scale of the cantilever specimens. A micro-gripper (FT-G102; FemtoTools GmbH) was also installed on the nano-positioner. The gripper had an opening range of 0–100 μm; the gripping force was controlled with a resolution of 0.5-μN via a sensor attached to one of the two gripping arms. By observing the force signals from the gripper arms, it was possible to determine when the gripper arms touched the sample. This enabled us to

determine an appropriate gripping distance, ensuring that the sample was not damaged during manipulation. Thus, this set-up can be used to manipulate fiber bundle specimens that are impossible to handle with conventional FIB sample stages. The location of the two end-effectors was designed so as not to interfere with the operation of the other installed components. Thus, every device could be operated simultaneously with the ion-beam column and sample transfer stage. This set-up can be easily modified as needed by attaching or detaching end effectors from nano-positioners.

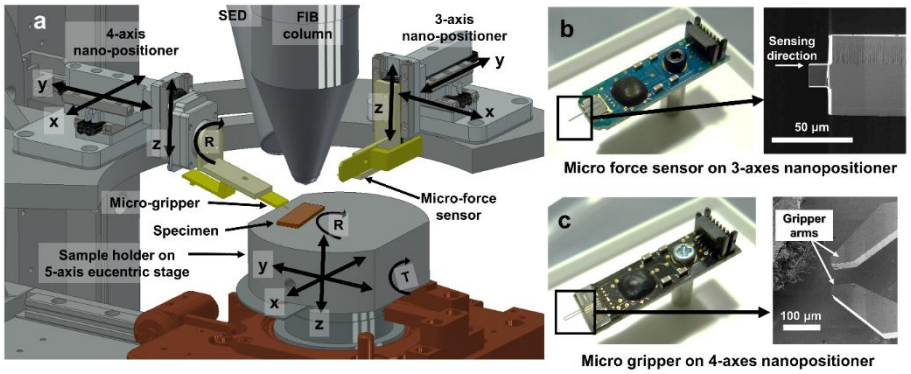

Figure 16 Design of the system used to measure micro-mechanical properties in a focused ion beam (FIB) system

To evaluate and compare the mechanical properties of exocuticle and endocuticle layers in the beetle horn shell, cantilever-shaped samples were

fabricated and bending tests were conducted. Figure 17 shows the process flow of sample preparation for in-situ experiments using the FIB system. A piece of shell was taken from the beetle horn and attached to the 4-axis nano-positioner on the specimen holder. In the case of the endocuticle layers, to fabricate a cantilever, part of the exocuticle layer was peeled off the procuticle layer with a sharp knife and placed on the nano-positioner. The cantilever shape was then fabricated using FIB milling in two orthogonal directions: from the top surface and sidewall of the layer. Due to the tilt angle limitations of the sample stages on conventional FIB systems (from −10° to +60° of pitch in general), it can be difficult to fabricate both sides without the sample reattaching. However, our proposed system does not have this limitation, as we can use the fully rotatable R-axis of the nano-manipulator in the direction of roll. With our system, the sample can be machined without its initial orientation changing during the fabrication process. We used a high current gallium ion beam (acceleration voltage: 30 keV; probe current: 10 nA) for rough structuring. Fine beams (acceleration voltage: 30 keV; probe current: 100–500 pA) were used for precise structuring. During the milling process, any protective layer was not covered except 10 nm of platinum coating which is used to eliminate the charging effect, because covering material itself can affect mechanical properties for bending test. Modification of mechanical properties induced by ion irradiation is widely researched phenomena and it is anticipated the damage of specimen is in the order of tens of

nanometers [51-54]. In our experiment, however, the specimen has dimension in microscale, 8–15 μm in width and 40–45 μm in height. Thus, we anticipate the damage accumulated near surface of specimen will not play a critical role of mechanical property change. Also, because the precise structuring process was performed at a very low angle of incidence, damage to the structure was expected to be minimized [42, 51, 55, 56]. In addition to the cantilever bending test for each layer, we performed a micro-bending test using a single fiber bundle. This enabled us to explore the mechanical properties in more detail. Figure 17 also shows the sample preparation procedure used for the single fiber bundle bending test. To take a bundle of nanofibers from the laminated endocuticle layer, the endocuticle was torn into several pieces. We secured a single protruding bundle at the edge using the micro-gripper and then detached it using FIB cutting. The bundle of nanofibers was cut to a length of 100–150 μm and a diameter of 2–10 μm. The sample was fixed by the gripper during the bending test.

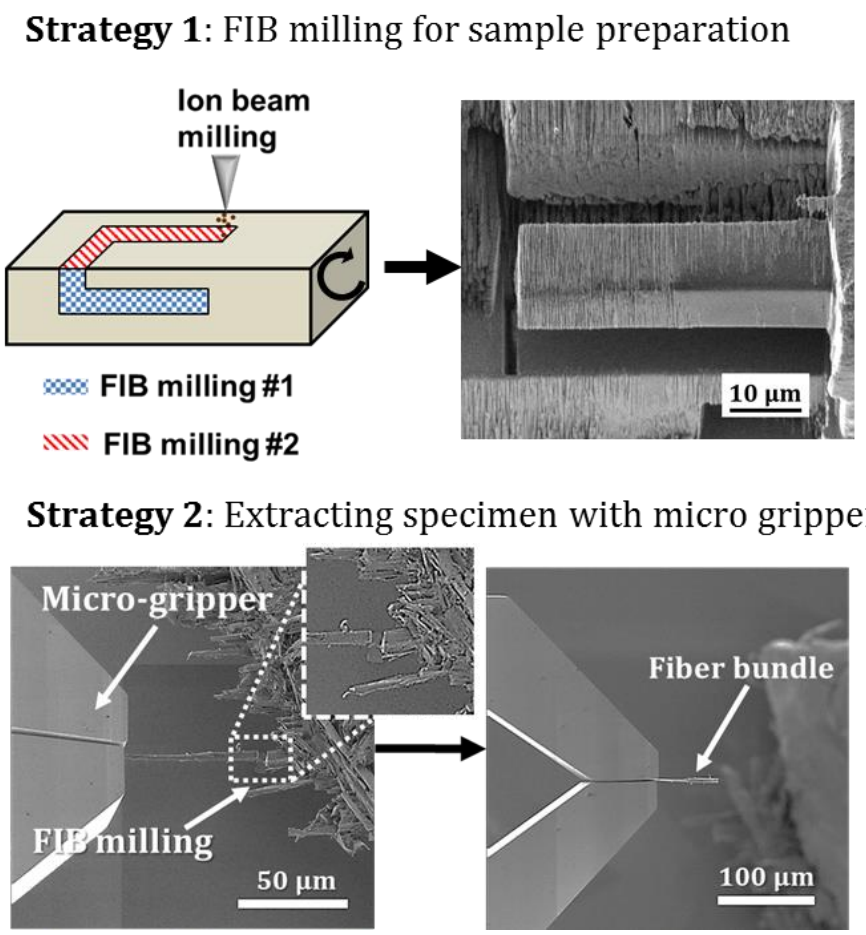

Figure 17 Sample preparation for microscale bending test of specific site of beetle horn shell

During the bending tests, a load was applied to the end of the cantilever (or bundle of nanofibers) using the tip of the micro-force sensor. The load was within or over the elastic deflection area. The pushing speed of the sensor tip was 40–50 nm/s. The reaction force and deflection data were

logged by a controller (MCS-6C-IDESH; SmarAct, Oldenburg Germany) with a 50-ms sampling time. The entire experimental process was observed using a secondary electron detector (SED) with a side view of the FIB system. From these microscopic images and data, we verified that the bending motion occurred in an orthogonal direction. Thus, we were able to check for elastic deformation or failure of the sample in real-time.

Figure 5 and Figure 6 show one set of the maximum stress-strain curve of the in-situ exocuticle and endocuticle bending tests, respectively. In addition, behavior of each samples during the bending motion are observed with real time images. The maximum tensile stress and tensile strain occur at the top of the cantilever beam during the cantilever bending motion. Based on these bending results, the Young's modulus (E) and stress (σ) were derived using simple calculations based on the equation,

$$E = (P \cdot L^3/3 \cdot \delta \cdot I)$$

$$\sigma = P \cdot L \cdot h/2I$$

$$I = w \cdot h^3/12$$

Values for the deflection (δ), load (P), length (L), inertia (I), width (w), and height (h) were determined from data collected by the force sensor and FIB imaging. The E was obtained by extracting the initial linear part of the graph.

The measured E of the exocuticle layer was 9.03 GPa and the fracture

strength was 533.6 MPa in average. As shown in stress-strain graph and real time images (Figure 18), the behavior is similar to that of homogeneous, brittle materials. As the cantilever bending deflection increased, fracturing was initiated at the fixed end of the cantilever. This collapsed the structure as the crack grew. The Young's modulus of the endocuticle layer was 4.97 GPa and the fracture strength was 245.3 MPa in average and each samples has large deviation by the samples (3 – 7 GPa) as shown in Fig.9. In addition, the deflection behavior of the endocuticle layer was different from exocuticle layer. In the early stages of repeated bending with small displacement, the stress-strain curve exhibited general elastic deformation behavior. However, as the deflection increased, the general bending trend did not continue. There were several sudden reaction forces, providing strong evidence of crack generation. Although crack initiation was observed several times during bending, the entire graph did not indicate structural collapse. The linear deformation trend continued once the sample was bent beyond a particular lateral region. When cracks were generated and the structure collapsed, the fatal cracks were not at the top surface of the fixed end of the cantilever, where the maximum stress occurs. The cracks appear along the direction of the fiber bundle, especially between the fiber bundles (Figure 19). When the structure collapsed due to the cracks, the fiber bundles were not cut and the cracks were blocked at the boundaries of the fiber bundles, so did not spread to the adjacent bundles. This prevented stress concentration and

lateral crack growth.

This effect is known as crack blunting, which occurs in fibrous endocuticle layers [57] and this hypothesis is supported by microscopic images of various samples with different fiber direction (Figure 20). The factures occur along the direction of fiber bundle. In the endocuticle layers, a fatal fracture that causes structural failure will not occur when the fiber bundle is snapped but when cross-links between fibers become disconnected. The mechanical properties of a fiber bundle from the endocuticle layer were measured in the same way (Figure 21). The samples were cut as approximately 60-80 μm in length, similar to cantilever bending samples, and measured beam thicknesses were 1.5 – 5 μm. The modulus shows wide variation by samples and no evidence related to crack initiation or fracture generation was observed in the measured data and the microscopic images, in about 20 μm of deflection. Comparing the endocuticle layer, some fiber bundles were tougher than endocucitle layer, which is an assemble of bundles; we note that facture occurred at 2 – 8 μm of deflection in case of the endocuticle layers. This is why, when cracks were initiated between the fibers bundles, the entire structure were not collapse at one time during the bending test in endocuticle.

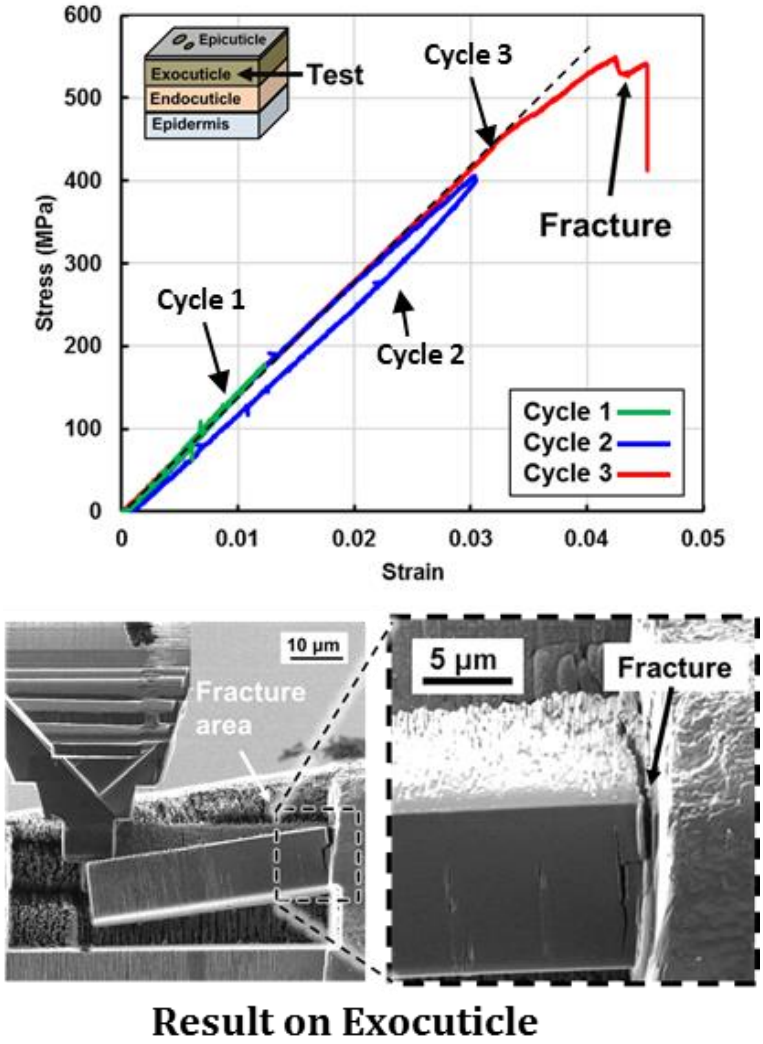

Figure 18 Result of bending test on the exocuticle of beetle horn shell [58]

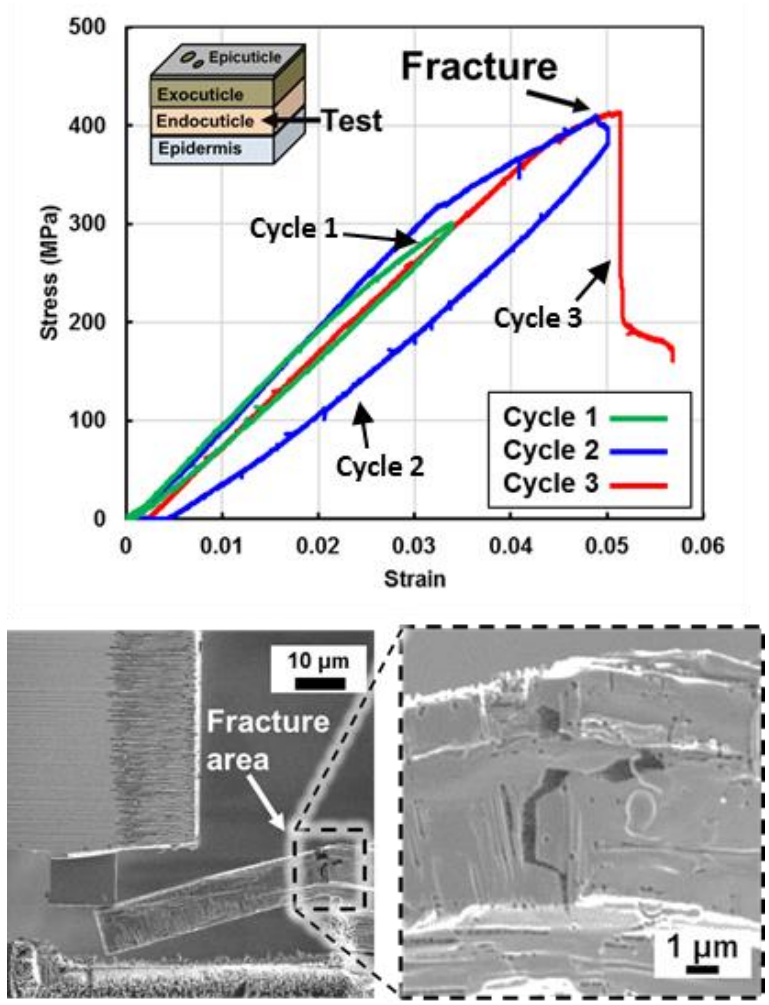

Figure 19 Result of bending test on the endocuticle of beetle hornl

[58]

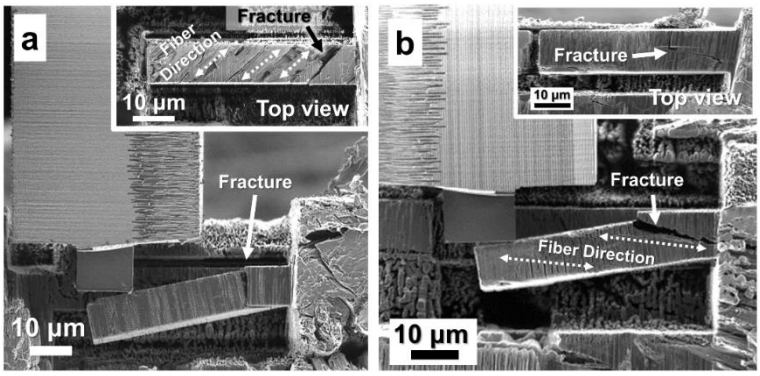

Figure 20 Examples of microscopic images taken at fracture during the endocuticle layer bending test [58]

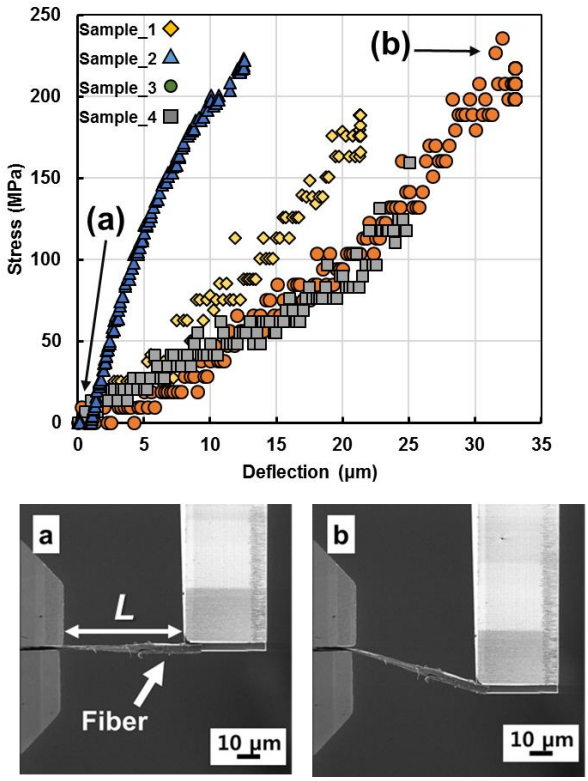

Figure 21 Result of bending test on the single fiber bundle extracted from endocuticle of beetle horn shell [58]

Chapter 3. Fabrication and evaluation of SMA microstructure

3.1. Test platform

To evaluate the shape memory effect in the fabricated structure, deformation and heating tests were conducted on the test platform. The test platform for the stretching test is shown in Figures 22 and 23. Two nanopositioners were attached in opposition on the base plate. Samples were attached at one nanopositioner and a micro-gripper or micro-force sensor was installed at the nanopositioner on the other side. The sample can be fabricated using focused ion beam (FIB) milling, on all sides and in the direction of rotation, with the aid of a fully rotatable R-axis nanopositioner. The platform can also be installed in the vacuum chamber of an FIB system and can operate simultaneously with FIB.

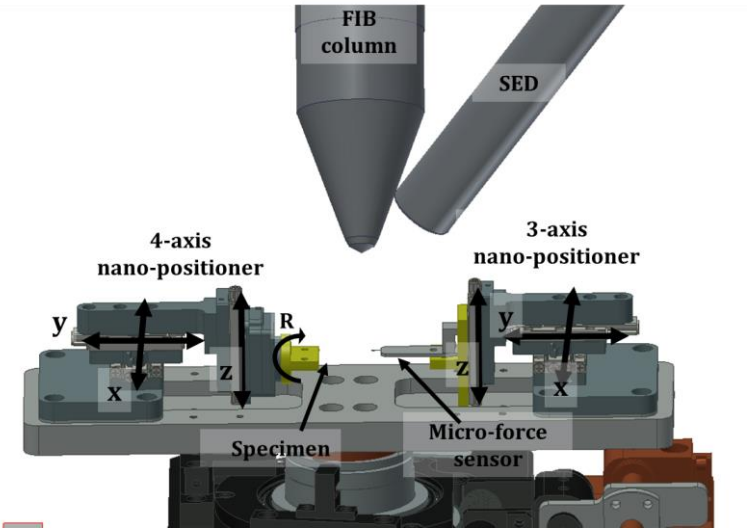

Figure 22 CAD design of in-situ nanomanipulation platform for stretching test

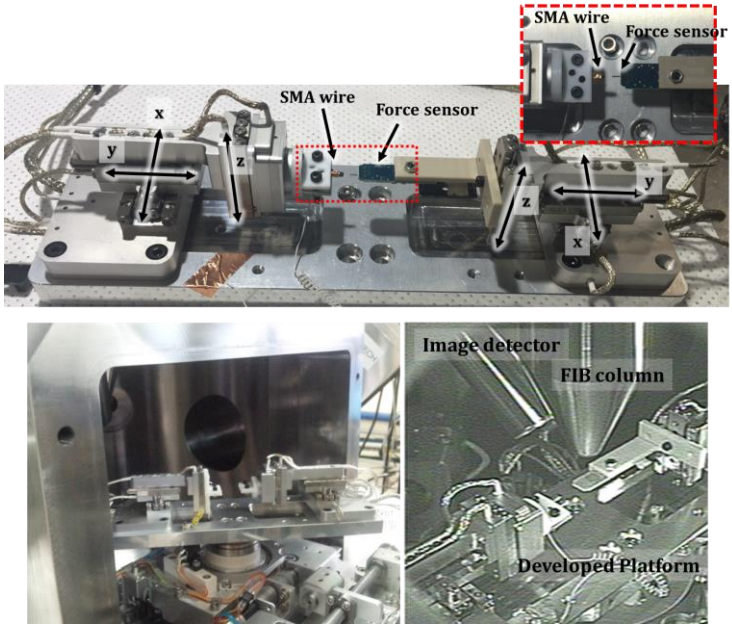

Figure 23 Picture of the developed platform and install in the vacuum chamber for FIB system.

3.2. Thin film fabrication using FIB milling.

Nitinol wire (25 μm in diameter) was purchased from Dynalloy, Inc. (Costa Mesa, CA, USA) The entire sample fabrication process was conducted on the in situ manipulation platform in an FIB system. One end of the wire was fixed to the jig, while the other end remained free. A schematic of the sample fabrication process is presented in Figure 24. First, the wire was milled into a thin plate (~1.5 μm thick). High ion dose conditions (probe current: 4,768 pA, acceleration voltage: 30 keV) were used initially for rough structuring. Then, lower ion beam conditions were used for fine milling (probe current: 719 pA, acceleration voltage: 30 keV). After finishing the wire-thinning process, the sample was rotated 90° in the axial direction so that the side wall was directed upwards and the FIB milling process could take place in this plane. Various designs can be patterned simply by projecting target patterns onto the milling area, with no post processing. A detailed process for the patterning is described in the following sections.

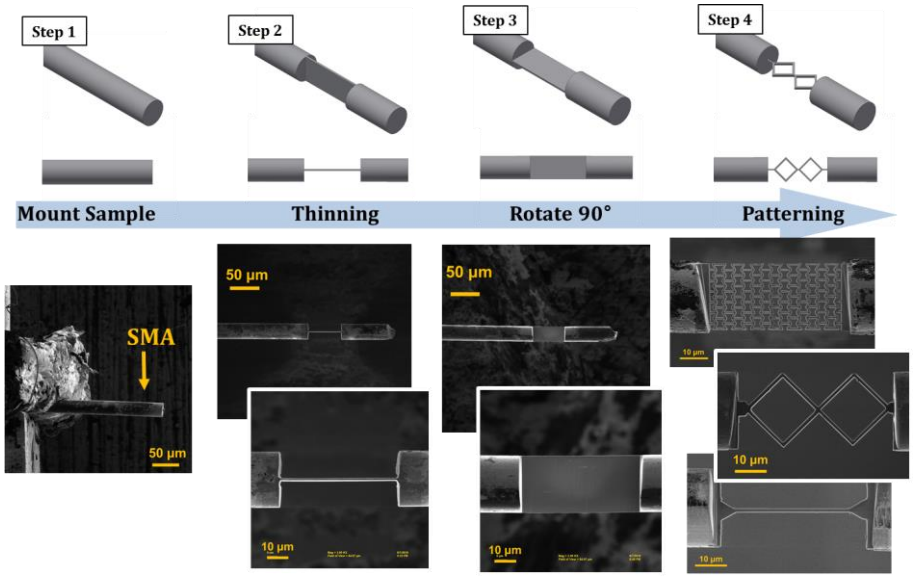

Figure 24 Process flow of sample fabrication for micro patterning with SMA micro-wire

3.3. Patterning method in FIB milling process

On the surface fabricated by the FIB thinning process, various shapes were patterned. Target shapes were drawn in black and white bitmap images where the white area is the maximum dwell time zone and the black area is the minimum dwell zone. Figure 25 shows an example patterning process done in an FIB system. For patterning, a low beam current (700 pA) was used to achieve precise pattern geometry.

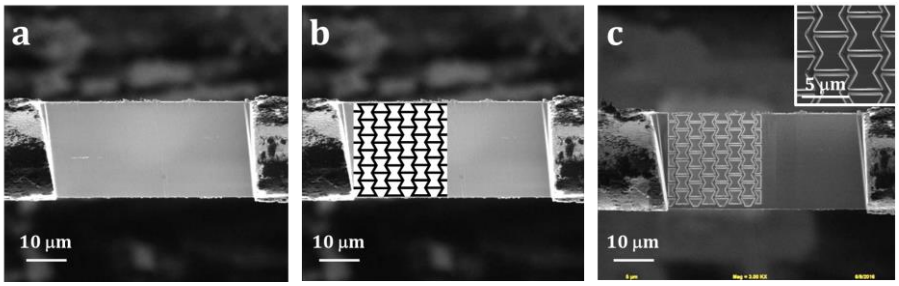

Figure 25 Example of bitmap image based pattern writing for FIB milling

Multiple diamond-shaped springs were patterned for developing a microactuator and robot. This diamond shape could be fabricated readily. Additionally, we could control the mechanical properties, such as the reaction force under stretching or maximum elongation, simply by changing the number of cells, the angle of the unit cell, or the structure

thickness. Figure 26 shows an example scanning electron microscopy (SEM) image of a microscale SMA spring having two cells with 90° of cell angle.

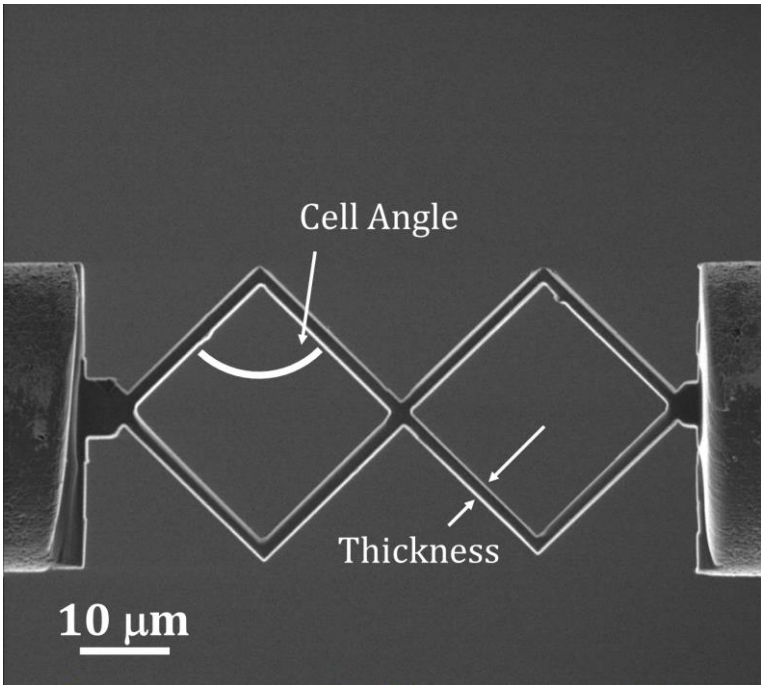

Figure 26 SEM image of microscale SMA spring structure having two cells with 90 degrees of cell angle

3.4. Prediction of damages at the surface caused by FIB milling process

Because the FIB milling process uses highly accelerated gallium ion beams (typically with 30 keV of acceleration voltage), the surface layer of a target material may be damaged. Researchers have investigated such FIB damage, as well as artifacts to control tit. The damage varies mainly according to the acceleration voltage and ion incident angle [59-62]. Kato reviewed the damage depth caused by an ion beam according to various beam energies (Figure 27). Mayer et al. investigated the damage occurring during ion beam milling by observing the generation of an amorphous layer on a silicon wafer (Figure 28) [60]. We can confirm the results of these previous studies: in this study, the damaged layer caused by ion beam milling was reduced as the acceleration voltage decreased and the thickness did not exceed 30 nm with 30 keV of acceleration voltage. Because the acceleration voltage used in this research was 30 keV, we can assume that the damaged layer will be < 30 nm thick.

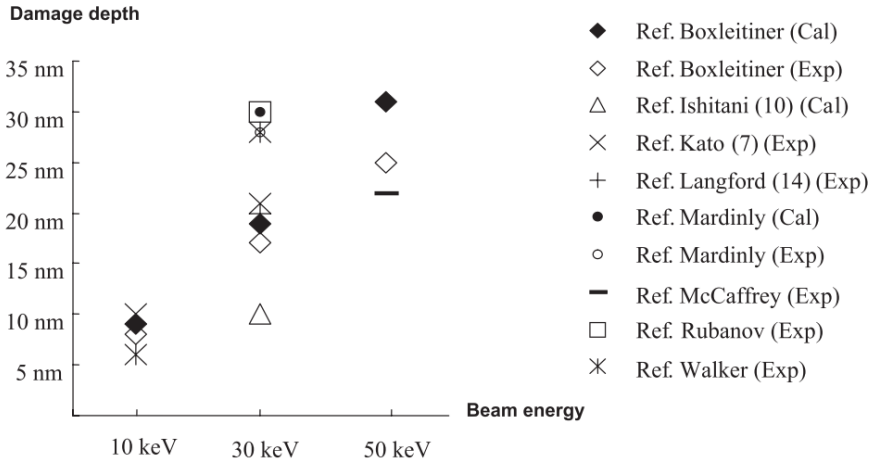

Figure 27 Damage depth of the FIB-prepared silicon foil as a function of the incident ion beam energy [59].

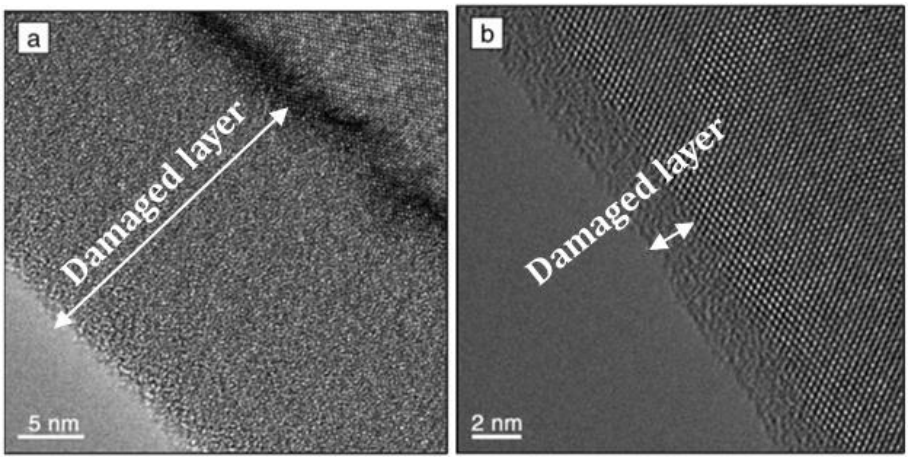

Figure 28 TEM images of the amorphous layer thickness in a sidewall of Si. (a) 30 keV and (b) 5 keV ion energy results in amorphous layers of ~22 nm and 2.5 nm thickness, respectively [60].

In addition, the thickness of the damaged layer has been studied by several researchers according to changes in the ion incident angle. Mikmeková et al. examined FIB-induced damage with low-energy SEM and estimated the sputtering yield and damage depth using a Monte Carlo simulation program called 'SRIM.' [61] (Figure 29). Fu et al. tested the effects of incident angle variation during FIB milling of water ice. [62] (Figure 30).

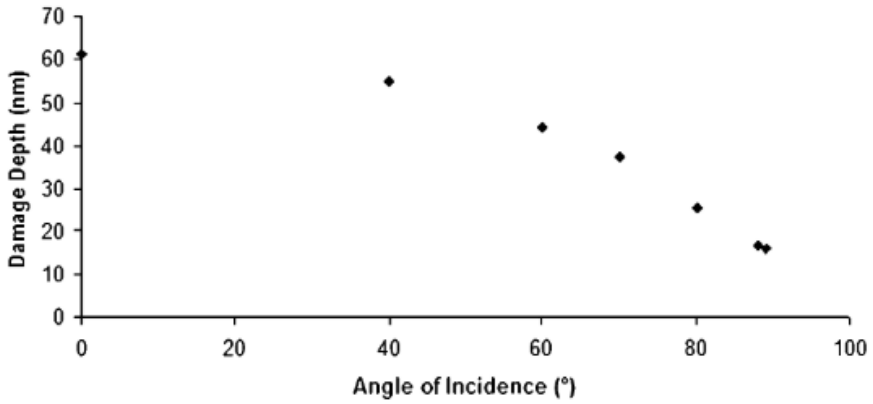

Figure 29 Calculated damage depth as a function of the angle of incidence [61]

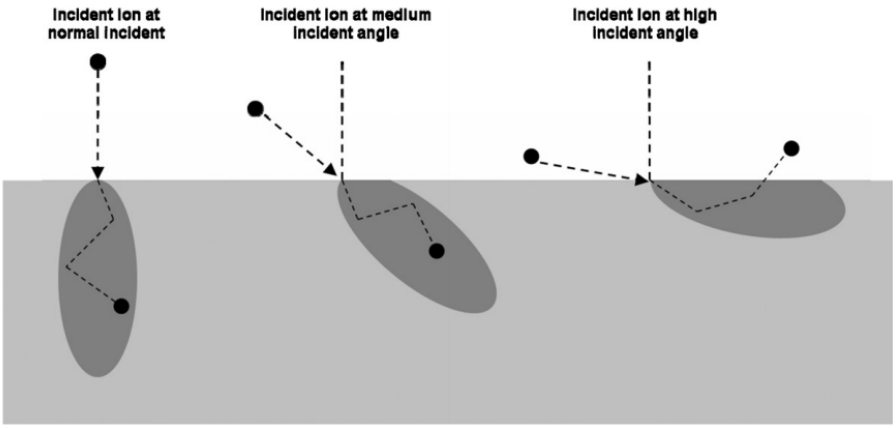

Figure 30 Schematic diagram of the effective region of ion track at different incident angles [62]

In this research, the fine milling process was performed at an incident angle of almost 90°, so we can assume that the damage due to Ga impact was minimized. Additionally, the thickness of the damage caused by ion bombardment on the NiTi material was estimated using SRIM. The Ga penetration depth at NiTi with 30 keV of acceleration voltage was calculated at incident angles of 0° and 89.9°. As shown in Figure 31 and Figure 32, the Ga ion penetration depth was much lower in the high incident angle case. In addition, by comparing the results by ion intensity, as shown in Figure 33, we can conclude that the chance of damage is much lower in cases with a high indent angle; the depth of damaged layer was < 10 nm.

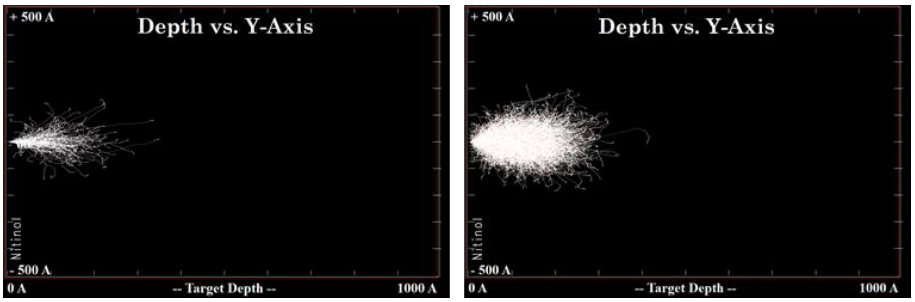

Figure 31 Simulation of the trajectories of 1,000 (left) and 10,000 (right) Ga ions bombarding at normal incidence the NiTi surface

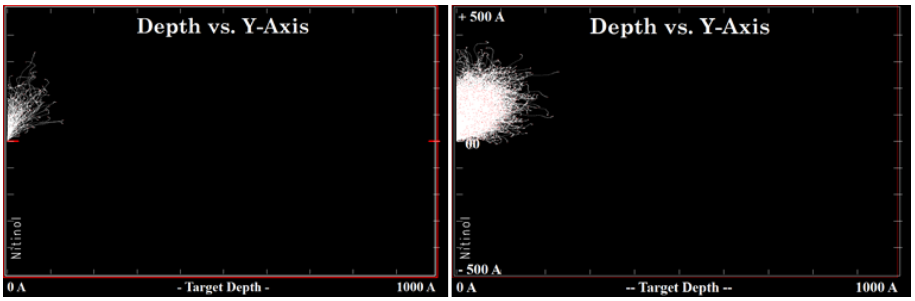

Figure 32 Simulation of the trajectories of 1,000 (left) and 10,000 (right) Ga ions bombarding at the NiTi surface with 89.9° of incident angle

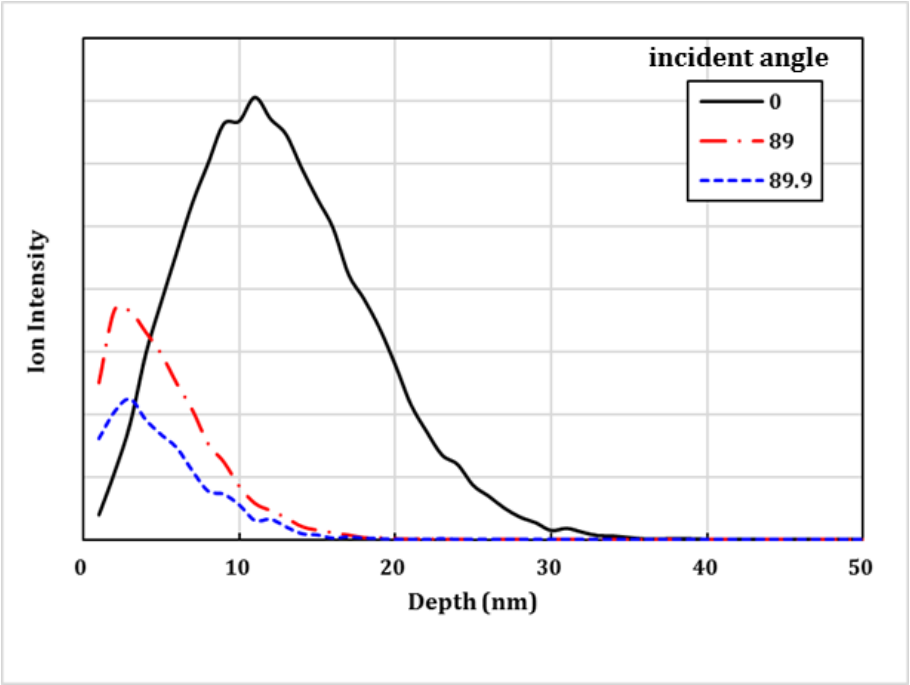

Figure 33 Ion Penetration depth and ion intensity according to the ion beam incident angle

Because we used a 30 keV acceleration voltage with a 90° beam incident angle for the fine milling process, we can assume that the damaged layer from ion beam irradiation is < 10 nm thick. When we consider that the thickness of the frame of the final diamond-shaped structure is 1–1.2 μm, the damaged layer represents only 1–2% of the entire structure so that it will not have much effect on the shape memory effect of the NiTi material.

3.5. Characterization of SMA cells

Figure 34 shows SEM images taken during a stretch test on the fabricated microscale SMA spring structure. To achieve deformation, the free end of the fabricated structure was hooked to a force sensor tip and stretched to a certain distance. During stretching, the stretching distance and reaction forces were logged by a data acquisition system. Real-time images of the sample can be obtained using the FIB system.

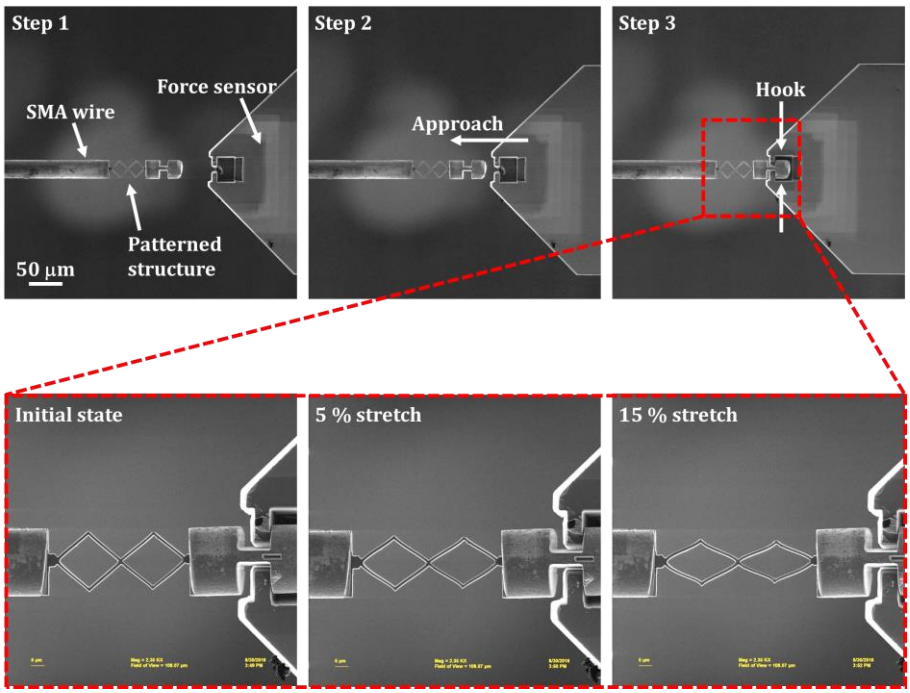

Figure 34 SEM images taken during the stretch test on fabricated microscale SMA spring structure

Figure 35 is a displacement-force graph for a stretch test of a 90° double-cell structure. As confirmed in the inset SEM pictures, the structure underwent large deformation. The elongation ratio was ~24% of the original length of the structure; this is much larger than the intrinsic elongation limit of non-patterned bulk SMA, which is typically 6–10%. With a 12 μm stretch length, the reaction force showed 400 μN approximately and the slope was non-linear.

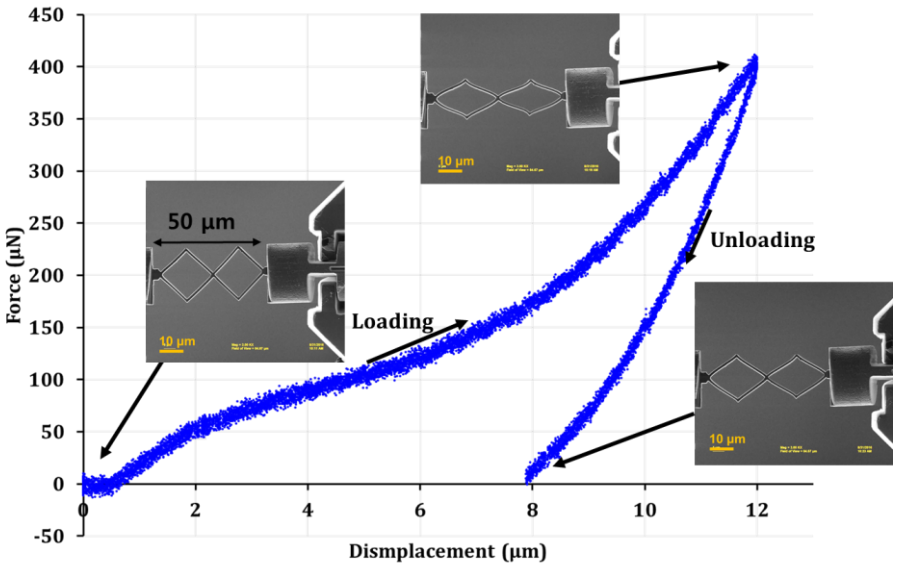

Figure 35 Load-Displacement diagram during the stretching motion of SMA spring pattern

This non-linear trend in reaction force is explained by a pseudo-rigid-body model, where the beam bends according to large deformation of a compliant structure [63, 64]. When dealing with a single frame of the spring structure as a fixed-guided beam (Figure 36), i.e., a beam that is fixed at one end, the other end is subject to deflection such that the angular deflection at the end remains constant, and the beam shape is anti-symmetric about the center.

The reaction force can be calculated with the following equations.

$$\mathrm{P} = \frac{4K_{\Theta}\mathrm{EI}\Theta}{l^2\cos\Theta}$$

Where P is a vertical force on beam and nP is a horizontal force.

$$\mathrm{a} = \mathrm{l}[1 - \gamma(1 - \cos\Theta)]$$

$$\mathrm{b} = \gamma \mathrm{l}\sin\Theta$$

$$\mathrm{K} = 2\gamma K_{\Theta}\frac{EI}{l}$$

$$\gamma = \begin{cases} -0.841655 - 0.0067817n + 0.000438n^2 & (0.5 < n \leq 10.0) \\ 0.852144 - 0.0182867n & (-1.8316 < n \leq -0.5) \\ 0.912364 + 0.0145928n & (-5 < n \leq -1.8316) \end{cases}$$

$$K_\Theta = \begin{cases} 3.024112 + 0.121290n + 0.003169n^2 & (-5 < n \le -2.5) \\ 1.967647 - 2.616021n - 3.738166n^2 \\ \quad -2.649437n^3 - 0.891906n^4 - 0.113063n^5 & (-2.5 < n \le -1) \\ 2.654855 - 0.509896 \times 10^{-1}n + 0.126749 \times 10^{-1}n^2 \\ \quad -0.142039 \times 10^{-2}n^3 + 0.58425 \times 10^{-4}n^4 & (-1 < n \le 10) \end{cases}$$

Or, for a quick approximation: $\gamma = 0.85$ and $K_\Theta = 2.65$.

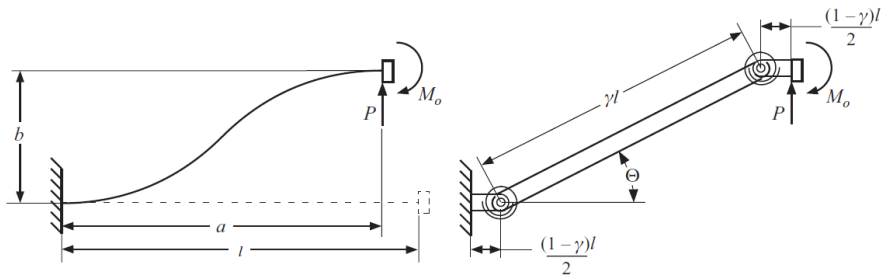

Figure 36 Pseudo-rigid-body model of a fixed-guided beam [64]

Based on this equations, a reaction force was calculated and compared with the experimental data. The values of a, b, and l were measured on SEM images taken during the experiment. As described in Figure 37, the calculated values agreed well with the experimental data, so we conclude that the reaction force during stretching can be predicted under various conditions.

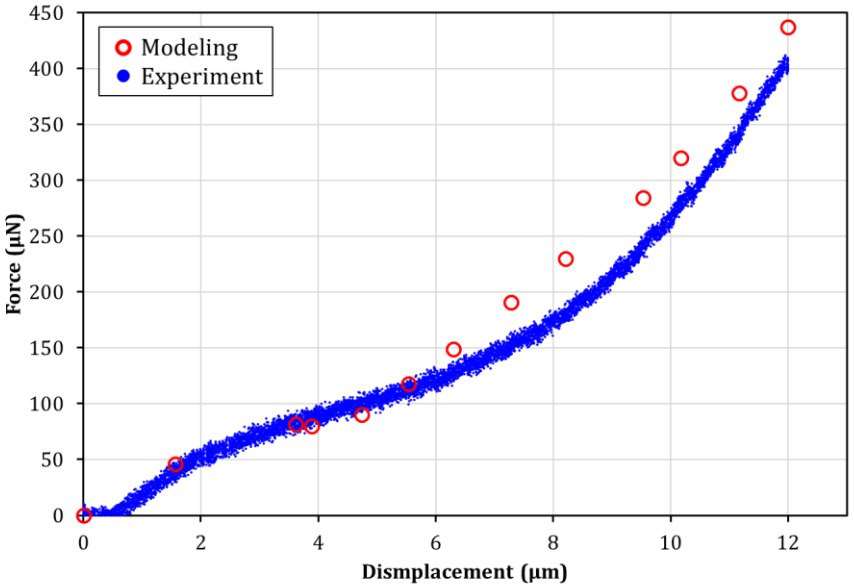

Figure 37 Comparison of experimental result and numerical modeling of the stretching motion of SMA spring pattern

3.6. Force depend on angle

To understand the change in reaction force according to the angle of the cell, various types of cell structure were fabricated and reaction forces were evaluated during stretching. Figure 38 shows various cells. In the same area (25 μm in height and 50 μm in width), 90°, 60°, and 30° cell angle structured patterns were fabricated to fit the patterning area. Then, the cells were stretched while measuring the reaction forces at the one end of the structure.

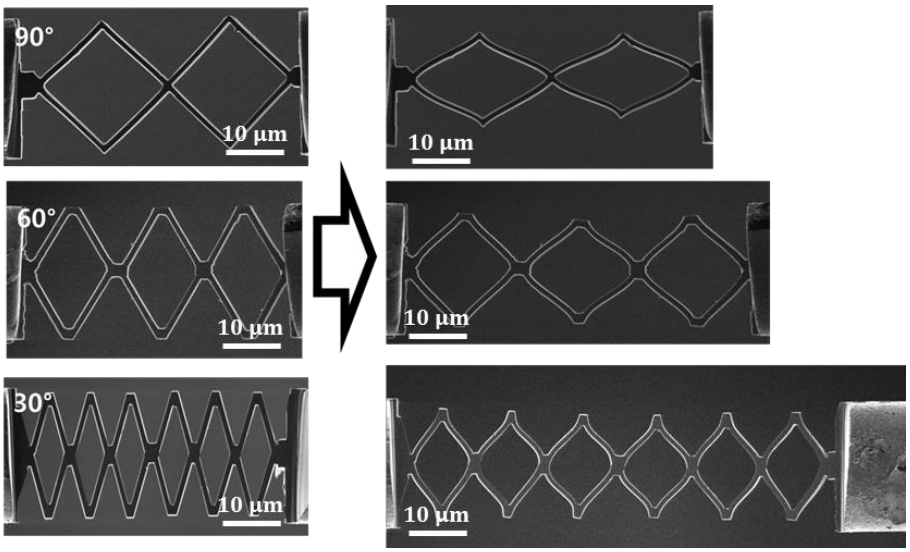

Figure 38 SEM images of SMA micro springs under stretching motion with various cell angle

The data were normalized in terms of the force, length, width, and thickness of the structure and the results are shown in Figure 39. At the same elongation ratio, the reaction force increases more rapidly for a sample with a smaller cell angle. Moreover, a structure with a smaller cell angle bears larger deformation. On stretching the structures, displacement and tensile forces were logged. As the stretching displacement increased, the reaction force also increased. The structure with 90° cells was stretched by 12 μm, which represents a 24% elongation over the original condition; the measured maximum unit force was logged as ~130 μN/μm2, whereas a structure with 30° cells showed 70% elongation and 150 μN/μm2 of unit force.

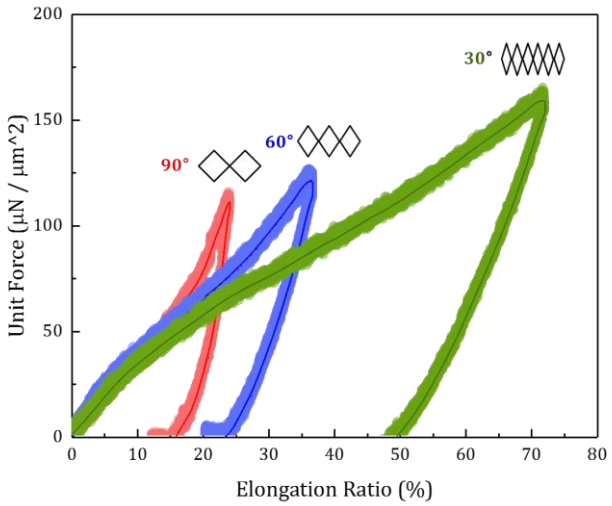

Figure 39 Reaction force change according to increase of elongation ratio and comparison in terms of cell angle

3.7. Investigation of deformation behavior with computational simulation

The deformation behaviors of fabricated structures were also investigated through a computational simulation method. Using the commercially available computational simulation software ANSYS 18 (ANSYS Corp., Canonsburg, PA, USA), mechanical responses during stretching of different structures were investigated. The material properties of the shape memory alloy components were set according to reference engineering data obtained in previous research (Table 2) [65] and the analysis conditions were set as described in Table 3. We can create meshes, specify the materials, mechanical conditions, and solution parameters, solve the calculations, view the results, and create reports using the built-in tools of ANSYS 18.

Table 2 Mechanical properties for shape memory effect analysis [65]

Parameter	Value
Young's modulus at Austenite	75,000 MPa
Poisson's Ratio	0.33
Material Hardening Parameter	500 MPa
Elastic Limit	300 MPa
Maximum Transformation Strain	0.08
Temperature Scaling Parameter	7.5 MPa/K
Load Dependency Parameter	0
Reference Temperature	273 K

Table 3 Analysis condition

Category	Condition
Geometry	90° 2 cells 60° 3 cells 30° 6 cells
Solver Target	Mechanical APDL
Analysis Type	Static structure
Materials	Isotropic Elasticity Shape memory effect
External Load	Fixed support Displacement
Solution	Equivalent strain Equivalent stress Reaction force

Regarding elongation of diamond-shaped frame structures, the experimental results shown in Figure 40 were compared with the simulation results in Figure 41. As shown in the graph, the simulation and experimental results were similar. Slight differences between the experimental and simulation results were caused by differences in the uniformity of the materials and small fractures or mismatches during structure fabrication.

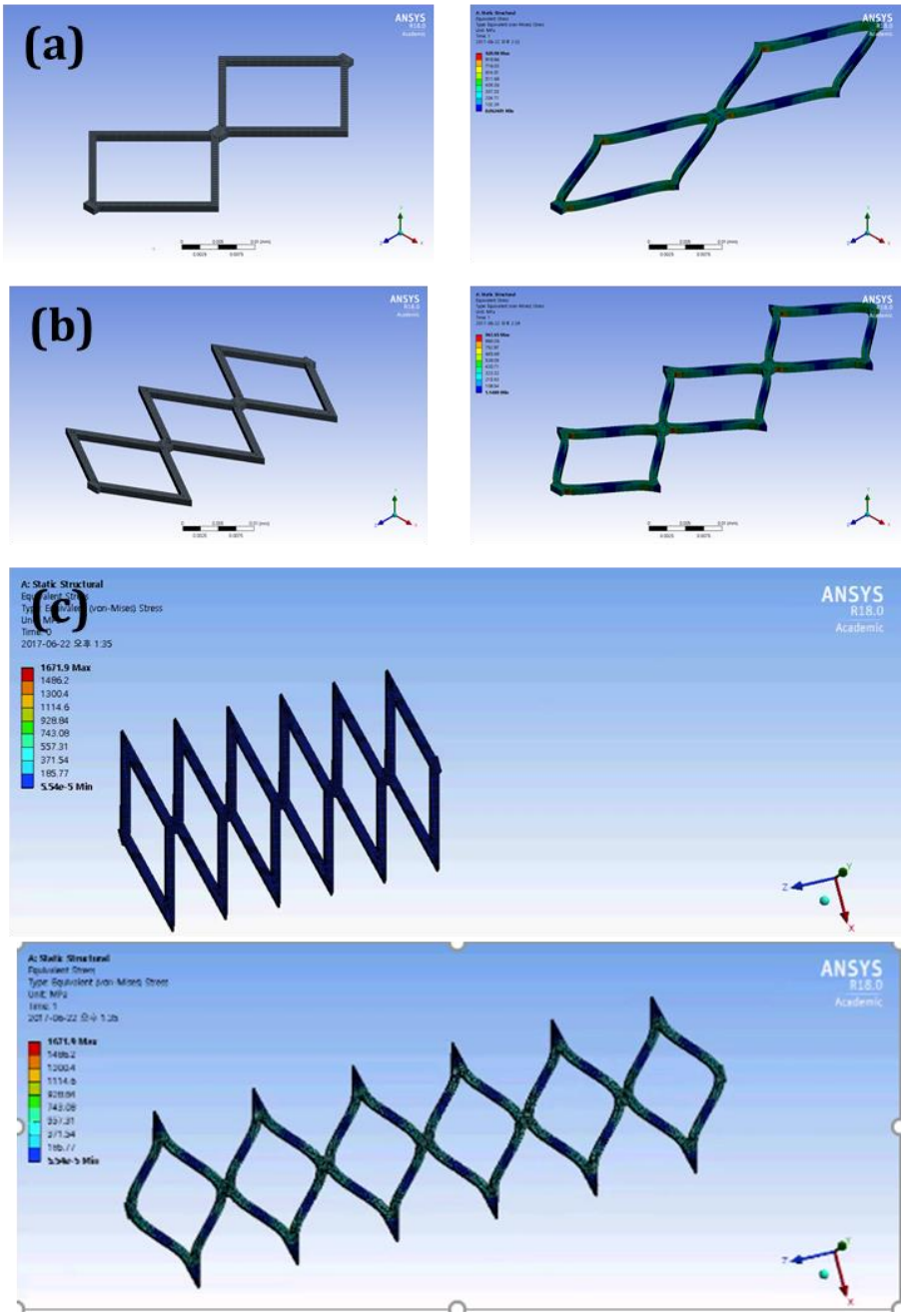

Figure 40 Result of ANSYS simulation of structural deformation of SMA structure (a: 90°, b: 60° and c: 30° structure)

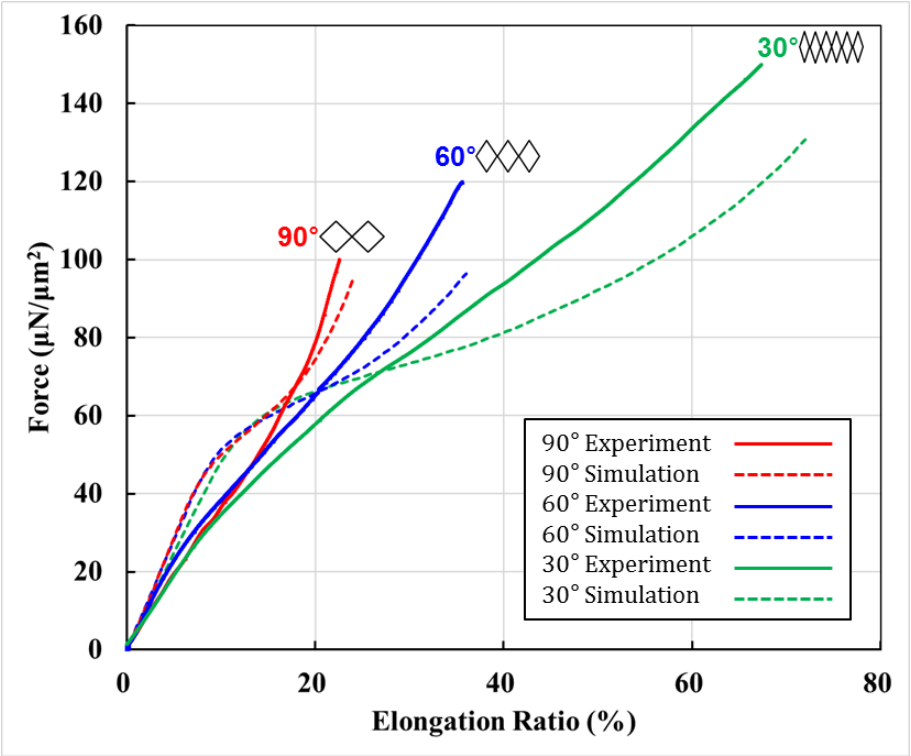

Figure 41 Comparison of experiment and simulation of reaction force under deformation

Chapter 4. Development of SMA based actuator.

4.1. Evaluation of shape memory effect.

It is known that shape memory effects in nitinol can be observed in extremely small structures, even at the submicron scale [25, 66]. To characterize the appearance of shape memory in our microscale structure, several experiments were conducted. First, differential scanning calorimetry was performed with bulk nitinol, as used in the experiment. Figure 42 shows the heat flow-temperature curves of the SMA. Two peaks are present due to latent heat absorption and release. M_s, M_p, and M_f are the martensite start, peak, and finish temperatures, respectively, during cooling. Similarly, A_s, A_p, and A_f are the austenite start, peak, and finish temperatures, respectively, during heating. The differential scanning calorimetry (DSC) curve shows that the nitinol we used had an austenite temperature of 69℃ on heating and changed back to the martensite phase between 20 and 30℃ during cooling.

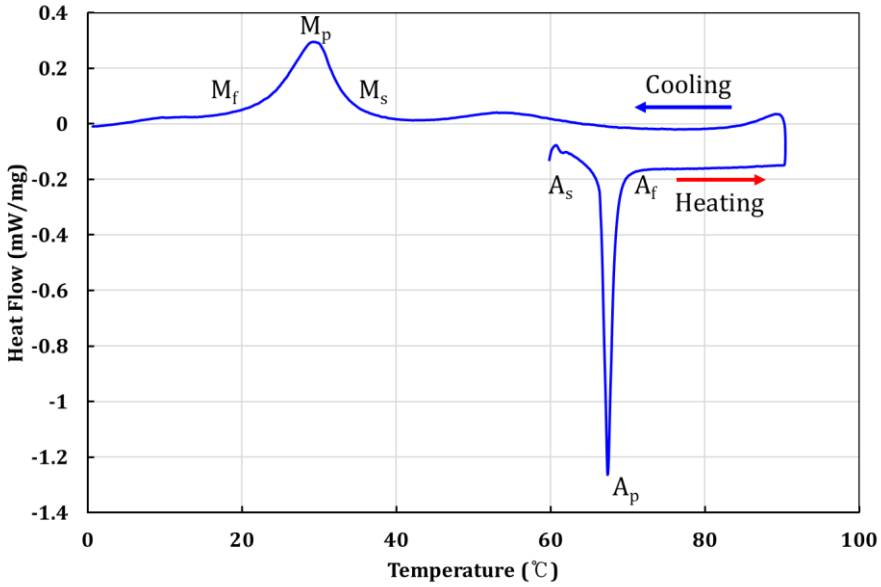

Figure 42 DSC curve achieved during the heating and cooling of SMA

4.2. Shape memory effect under ion beam irradiation condition

To observe the shape memory effect in the fabricated microscale structures, an in situ ion beam-induced heating experiment was performed within an FIB system. As shown in previous stretch tests (Fig 37 and Fig 39), once the structure was deformed, even though the stretching force was removed and the structure laid freely, the structure remained deformed and showed a degree of drawback. We presume that the entire structure underwent plastic deformation, and that this deformed structure would recover its original structure when heated due to the shape memory effect.

To this deformed micro-SMA spring structure, a high-energy ion beam (acceleration voltage: 30 keV, probe current: 4,768 nA) was applied. To increase the temperature in the structure while preventing ion beam damage to the sample, the ion beam was irradiated at the anchor of the structure. Once heat is generated by exposure to the ion beam, it will be transferred by conduction and the temperature of the structure will increase. As shown in Figure 43, the structure recovered its original shape after irradiation with a high ion dose.

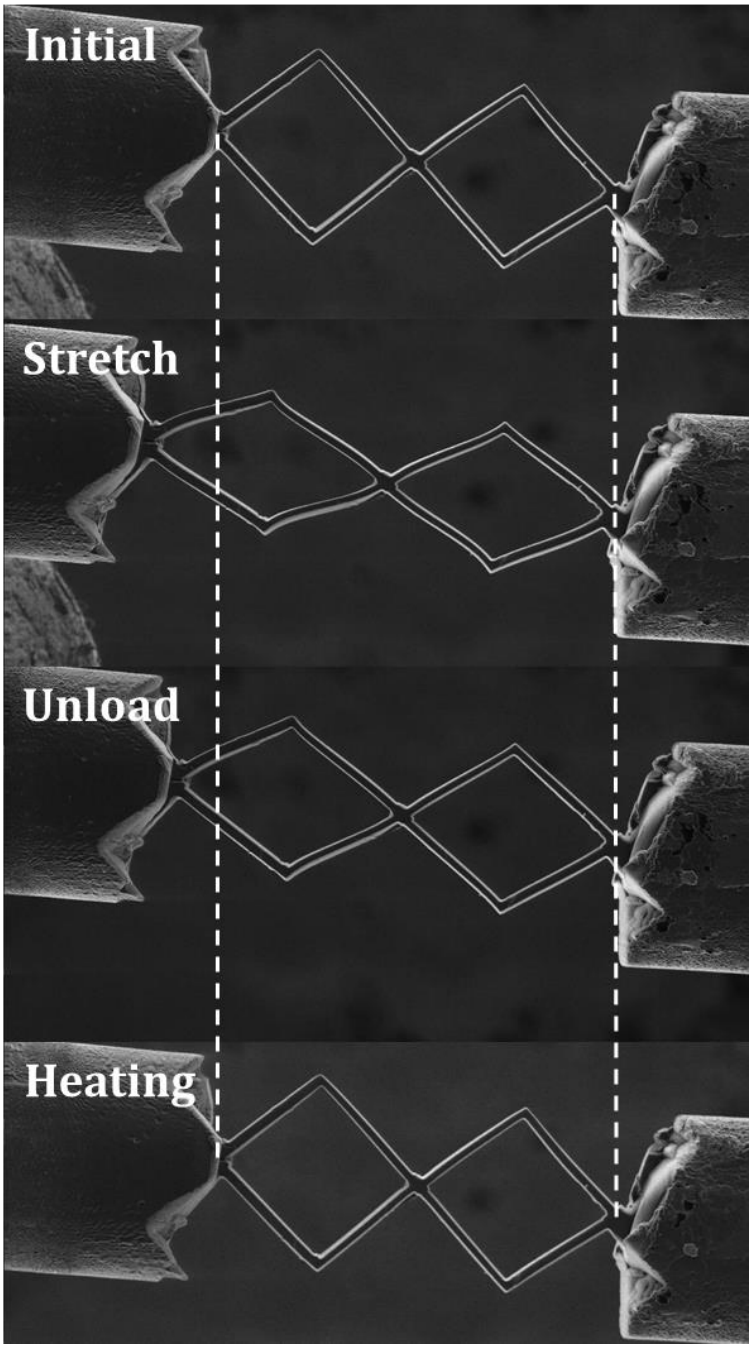

Figure 43 Real-time images of SMA spring patterns under stretching hang ion beam irradiated heating

Table 4 Beam irradiation condition used for ion beam induced heating

Condition	Value
Acceleration voltage	30 keV
Probe current	4.786 nA
Beam diameter	100 nm
Thermal conductivity of nitinol	18 W/m·K

The shape memory effect induced by ion beam irradiation was also evaluated by measuring the blocking forces. First, as shown in Figure 44, the reaction force of the stretched structure changed under ion beam irradiation; the fabricated microscale spring was stretched to a certain distance; then, the spring was released slightly and the ion beam was used to irradiate and heat the structure. Once the temperature rose above the phase transition temperature, the shape memory effect occurred and the structure sprung back to its original shape. However, in this case, the structure was fixed as stretched by a micro-force sensor and shape recovery effect was turned into a blocking force. This blocking force appears or disappears as the ion beam is switched between the on and off conditions, respectively. The switching speed was 200 ms and the force difference was 60 μN approximately. The reaction speed and force can be varied by heating conditions or structural differences; these variations will be discussed in the following sections.

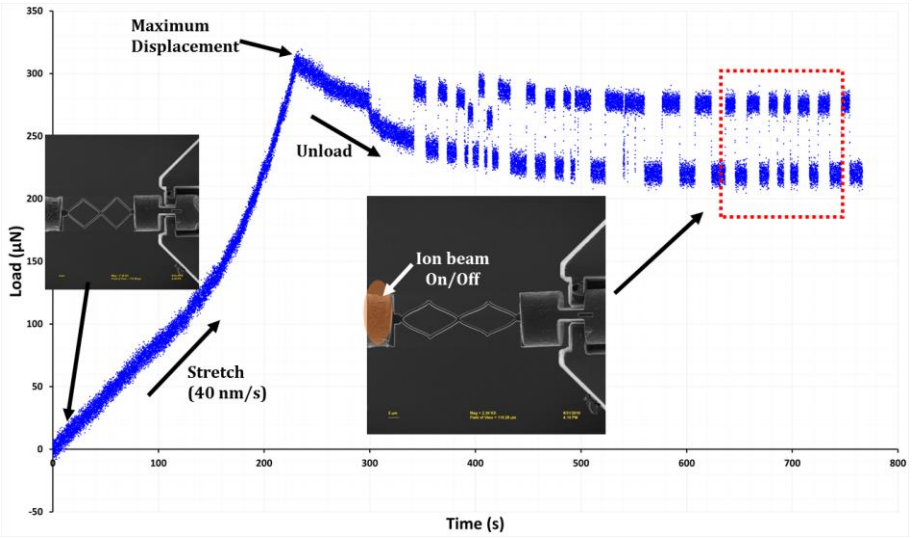

Figure 44 Reaction force change of stretched structure under ion beam irradiation

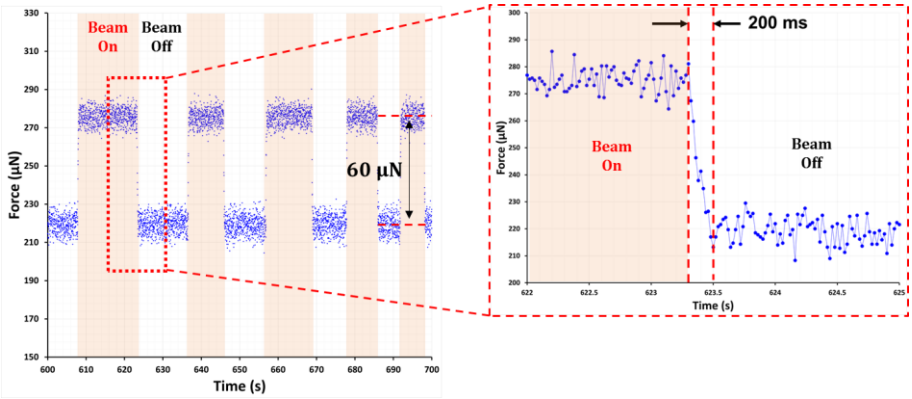

Figure 45 Measuring response speed under ion beam induced heating condition

When we compared the reaction force and the ion beam irradiation was synced to the time condition, we could confirm that the reaction force followed the ion beam irradiation well.

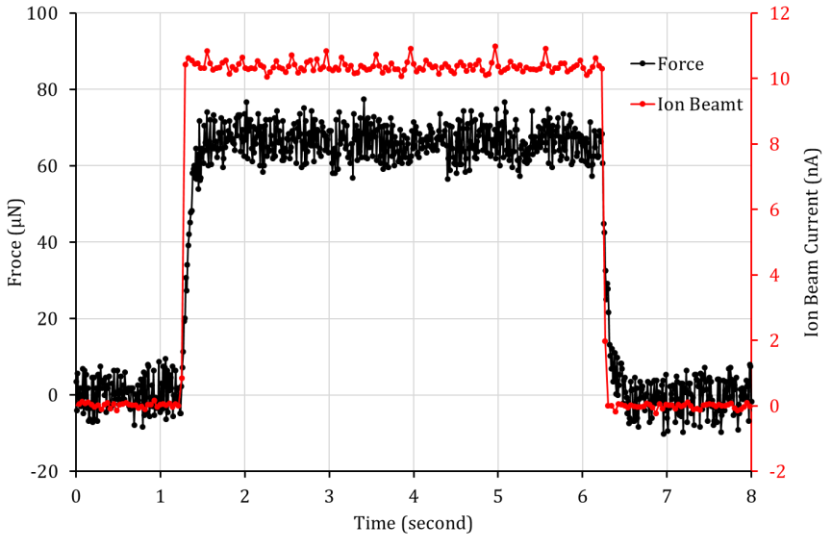

Figure 46 Diagram of reaction force change according to the change of the ion beam current

The ion beam-induced heating effect was also evaluated through a numerical simulation. Using ANSYS, the temperature increase under ion beam irradiation was calculated (Fig. 48). The computational simulation showed similar results to those of the experimental and numerical analyses.

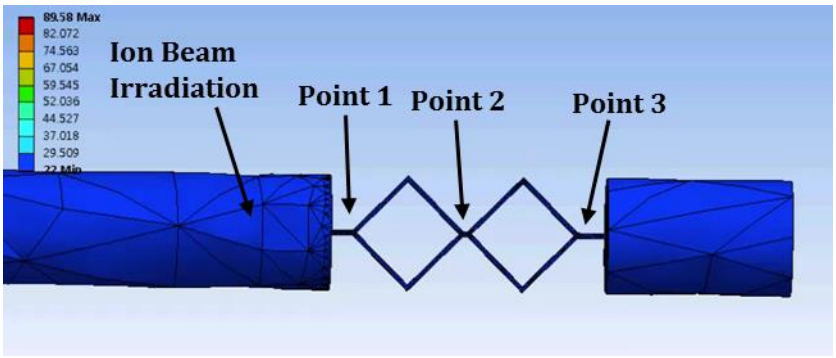

Figure 47 Image of structure model for numerical simulation with ANSYS

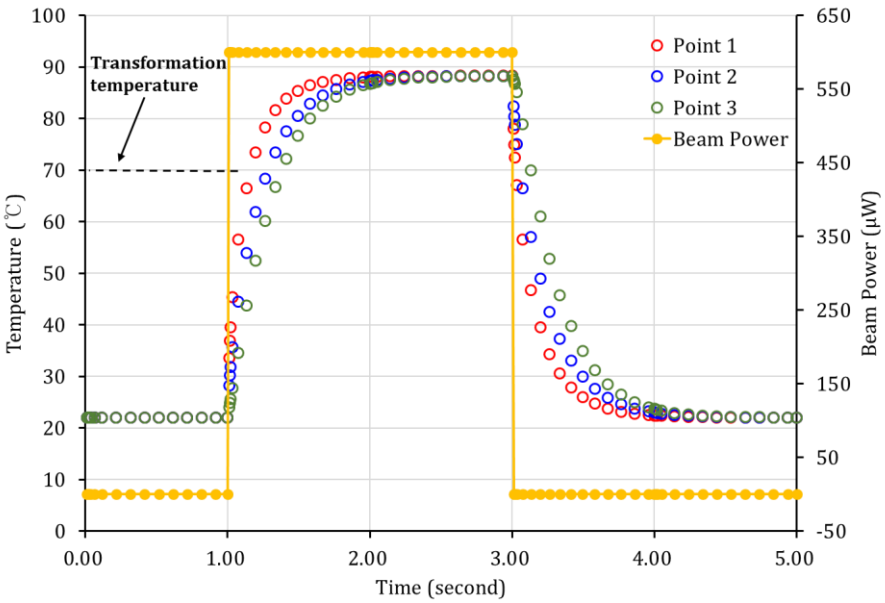

Figure 48 Result of numerical simulation regarding temperature rise by the ion beam irradiation

It is also known that the maximum temperature increase for a stationary beam can be expressed by the equation below [67], where the κ is thermal conductivity of target material, d is beam diameter, J is beam current density, I_p is beam current, V_a is acceleration voltage. Based on our calculations, the temperature increase in this experimental condition shown in Table 4 is ~90℃ and we can confirm that the temperature increase induced by the ion beam conditions used in this experiment overs the phase transition temperature of NiTi. According to our results, we can confirm that the structure still possessed a shape memory effect at ~1 μm thickness and ion beam-induced heat is thus an appropriate actuation method for a structure with a length of several tens of microns, if the structure is sufficiently thin.

$$\mathbf{T}_{max} = \{(2p/C_pD)/(2\pi)^{3/2}\}\{\pi/2\}$$

$$= \{(V_a/\kappa)/\pi^{1/2}\}\{I_p/d\}$$

$$= \{\pi^{1/2}\, V_a/4\kappa\}\{dJ\} = 90\ ℃$$

Because the temperature of the fabricated structure can be changed quickly, we can realize the SMA structure with a 10 Hz actuation speed by controlling the on and off status of the ion beam. This rapid increase and

decrease in motion, due to the scale effect, was measured (Fig. 49). The structure has an extremely small volume, so the heat capacity of the structure is also very small. Thus, we can change the temperature very quickly and this phenomenon can be used to drive fast SMA microscale actuation.

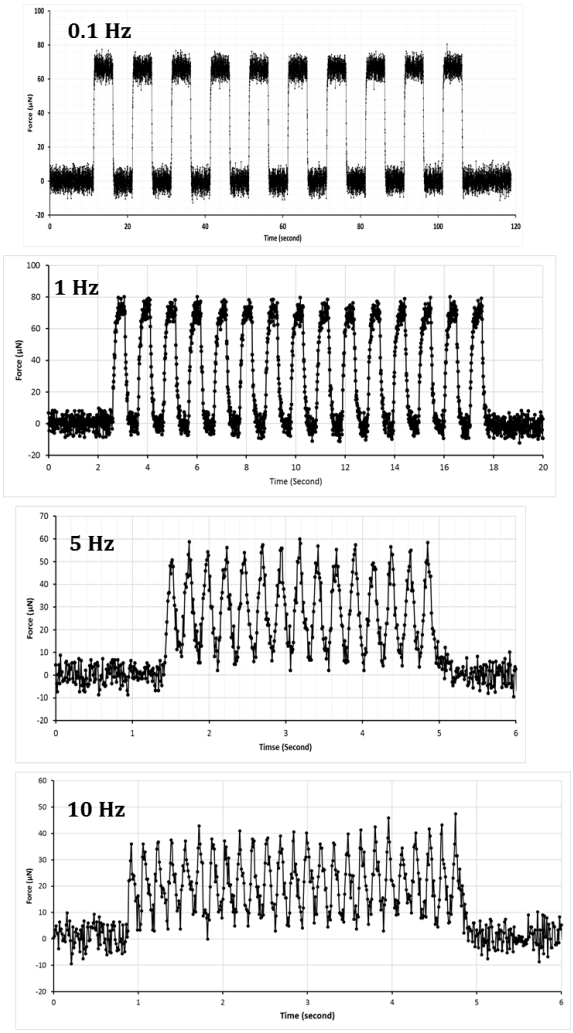

Figure 49 Measured reaction force of SMA structure

4.3. Shape memory effect under ambient heating

Phase transitions with an increase in temperature were also evaluated under ambient heating conditions. Placing samples on a hot plate at 100°C, a stretching test was performed and the results were compared with those obtained under ambient room temperature conditions. As described in Figure 50, the stretching test under heated conditions showed a higher reaction force due to a change in Young's modulus between the martensite and austenite phases. It is known that Young's modulus of the austenite phase (~83 GPa) is almost double that of martensite (~28-41 GPa), so that the reaction force also doubles.

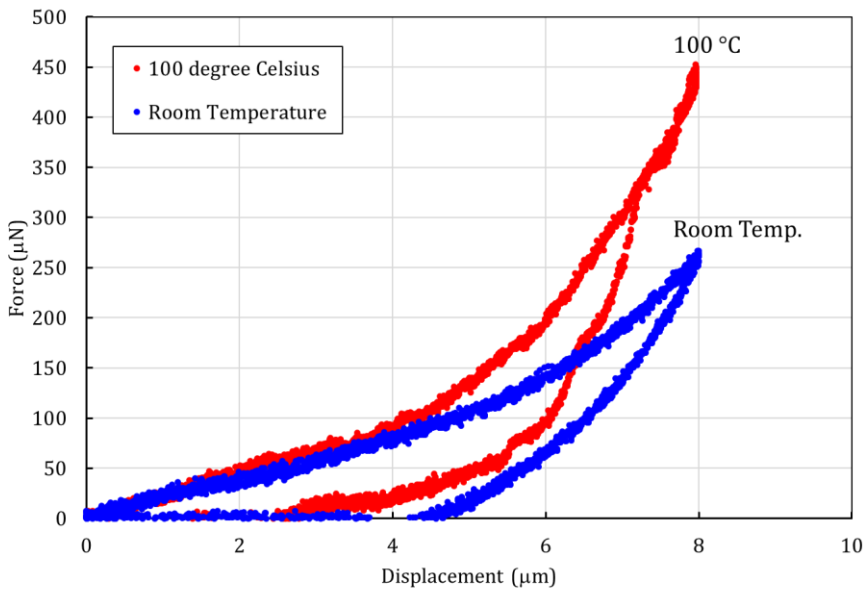

Figure 50 Comparison of increase of reaction force regarding the temperature difference

4.4. Shape memory effect with laser induced heating

Although the shape memory effect and actuation frequency were evaluated by an ion beam irradiation method in an FIB system, there were several limitations. First, the ion beam irradiation method can only be applied under high-vacuum conditions within an FIB system. Additionally, when we provide an ion energy that is too high to generate a higher power or faster response time, it sputters materials into the target area and causes permanent damage to the structure. As shown in Figure 51, the anchor of the fabricated structure was damaged and material sputtering occurred after repeated high ion beam irradiation. This structural damage is not repairable and has a negative effect on actuation. Because of this, we assessed an alternative driving source, i.e., laser irradiation, as a replacement for the ion beam irradiation method.

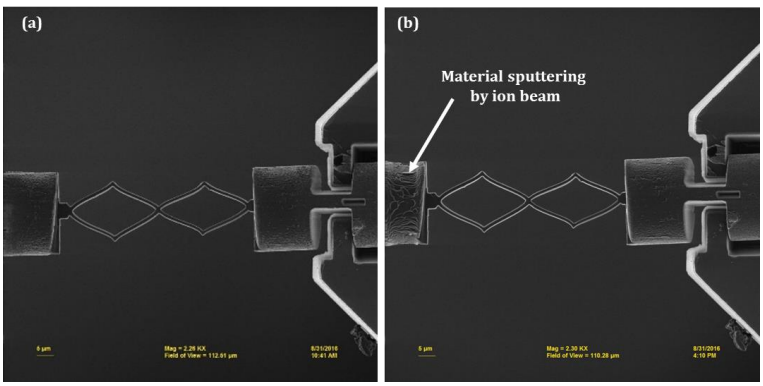

Figure 51 SEM image of SMA structures before (a) and after (b) actuation test under too large beam current

In the alternative method, a 355-nm ultraviolet (UV) laser source was used. UV-wavelength lasers are used widely for metal cutting due to its high energy-absorption coefficient against metals. As with all metals, NiTi also showed higher absorption in the UV region than in the visible or infrared (IR) regions of light. Additionally, a laser with a 355-nm wavelength possesses a small spot size and high pick power, and thus can be used as an alternative heating source for microscale SMA actuation. The light absorption ratio was measured on the NiTi used in this research with a UV-vis-near-infrared (NIR) spectrometer (Mega-2100; Scinco, Seoul, Korea) and the results are presented in Figure 53. As in previous research, the NiTi that we used showed a high absorption ratio in the UV range (near 355 nm) and we can conclude that the UV laser is one of the good candidates for driving source of the microscale SMA actuator.

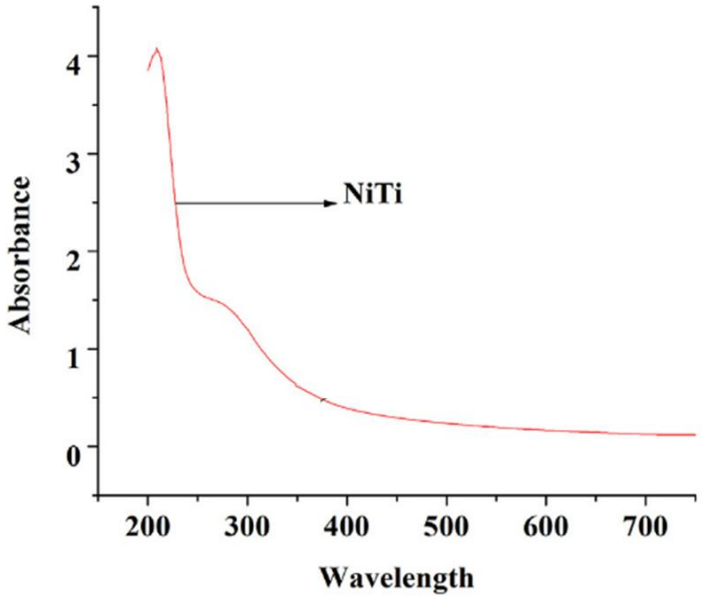

Figure 52 Absorbance spectrum of NiTi [68]

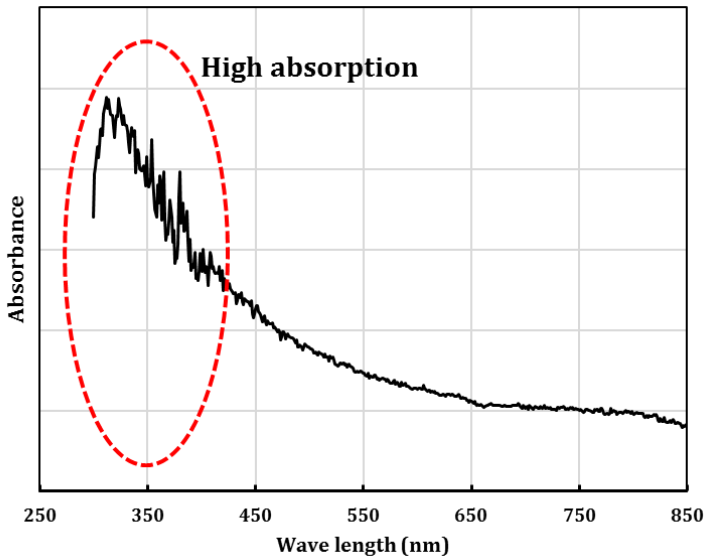

Figure 53 Light absorption ratio at NiTi used in this research

4.5. Development of hardware for laser-induced SMA actuation

The laser irradiation method can heat a specific area of the sample in the same way as FIB, i.e., by changing the focus area, and the beam can be switched on and off quickly. Additionally, compared with electrical activation, photothermal activation by light is desirable for contactless and spatially resolved control of actuation. Due to these advantages, using a laser irradiation method as the driving source allows for the development of a device that can operate under ambient conditions.

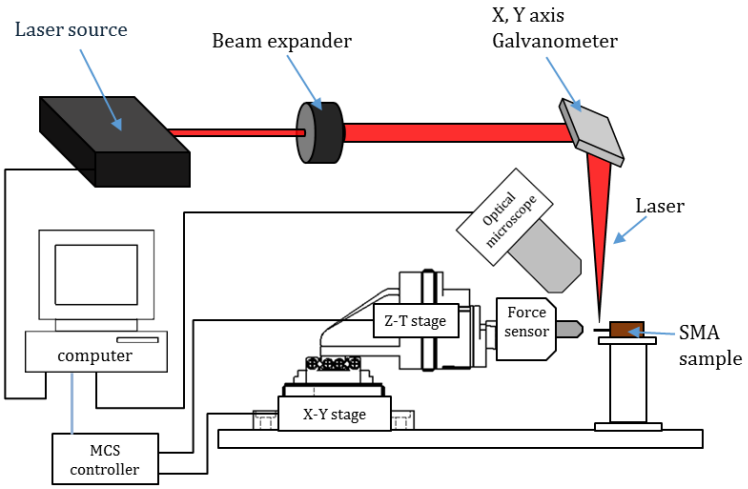

Figure 54 Schematic diagram of Laser irradiation system for SMA actuation experiment

Figure 54 shows a schematic diagram of the developed laser system and Figure 55 shows the evaluation set-up for measuring the SMA actuation

force. Similar to the in situ FIB manipulation platform, a micro-force sensor was attached at the end of a three-axis nanopositioner in the laser irradiation area. As in the experimental procedure for the FIB system, the micro-force sensor is hooked up to the SMA actuator so that the reaction forces generated by triggering the shape memory effect can be measured. The deformation of samples and location of the force sensor during the experiment can be observed by an optical microscope, rather than with SEM.

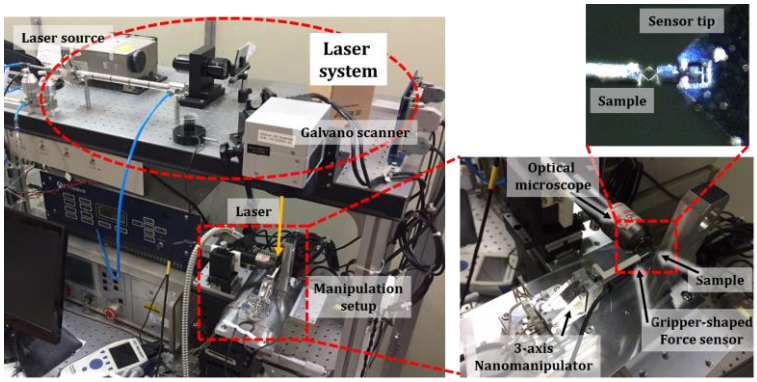

Figure 55 Picture of developed laser irradiation system

Figure 55 shows a detailed picture of the laser irradiation system. A UV laser with a 355 nm wavelength passes through the channel. The 0.7-mm intrinsic laser diameter was expanded with a beam expander to create an appropriate focus diameter at the target. The expanded laser passed

through the galvanometer attached at the end of the laser path. The laser irradiation position is controlled by the x-y galvanometer.

Although the galvanometer allows for switching the beam on and off, the frequency of switching is limited to less than ~300 Hz, so that we could not test a faster switching speed using the galvanometer alone. To overcome this, a rotational shutter was attached between the beam expander and the galvanometer (Fig. 56). As the shutter rotates at a certain speed (rpm), the laser path to the target is connected and disconnected repeatedly, which switches the status of laser irradiation on the target between on and off. Thus, we can change the switching speed readily simply by changing the speed of the motor connected to the rotational shutter.

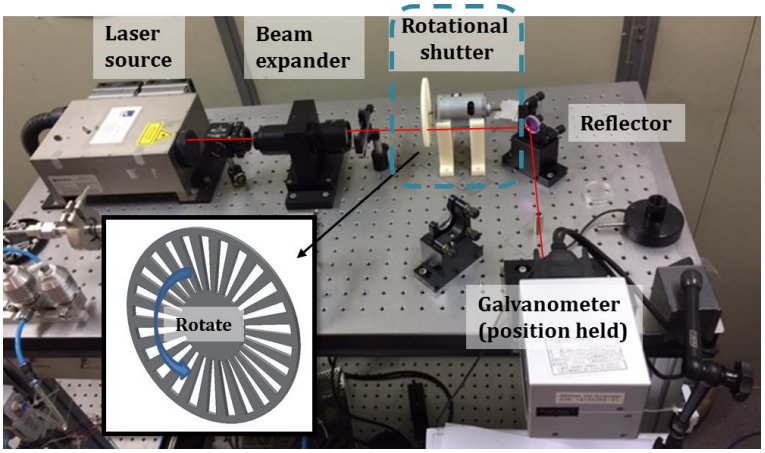

Figure 56 Picture of modified laser irradiation setup for high-speed beam switching

Chapter 5. Development of high-speed micro-actuator and robot

5.1. High-speed linear actuation

Figure 57 shows microscopic images of spring structures patterned with a focused laser. The experimental procedure is similar to that for the FIB system, comprising stretching, beam heating, and measurement phases; the only difference is in the beam irradiation location. In the case of the experiment with the ion beam, the beam was irradiated at the anchor of the structure, but in the case of the laser the beam is irradiated directly at the patterned area.

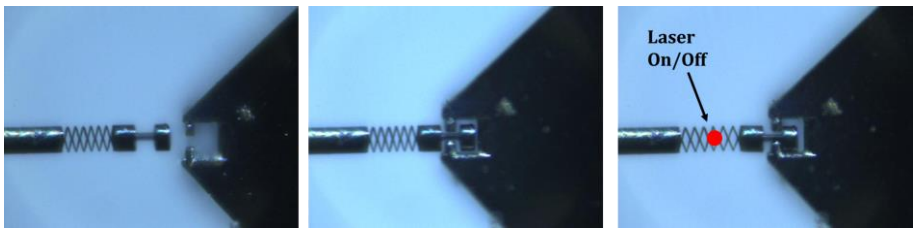

Figure 57 Microscopic images of force sensor and SMA actuator taken during the laser induced heating test

Another advantage of the laser-induced heating method is that we can control the actuation force readily simply by changing the laser power. The reaction force change according to variation in laser power was measured.

As shown in Figure 58, as the laser irradiation power increased from 5 to 60 mW, the reaction force increased and the rising rate of the reaction force also became steeper. When the laser power reached > 30 mW, the maximum reaction force became saturated and did not increase further. Although the reaction force did not increase over 30 mW of laser power, when we look more closely at the initial part of the graph, it can be seen that the response speed became faster up to the 50 mW laser condition.

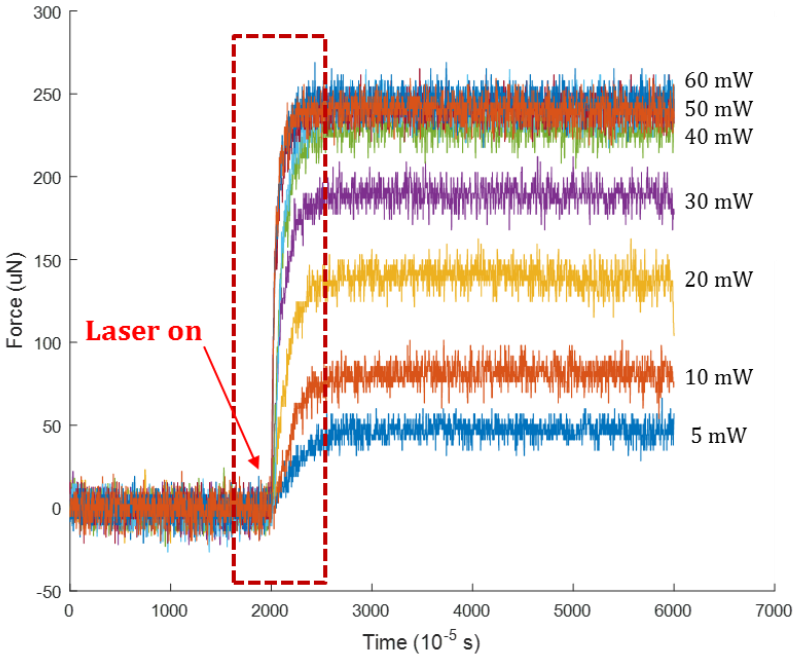

Figure 58 Increase ratio of reaction force according to change of the power of laser

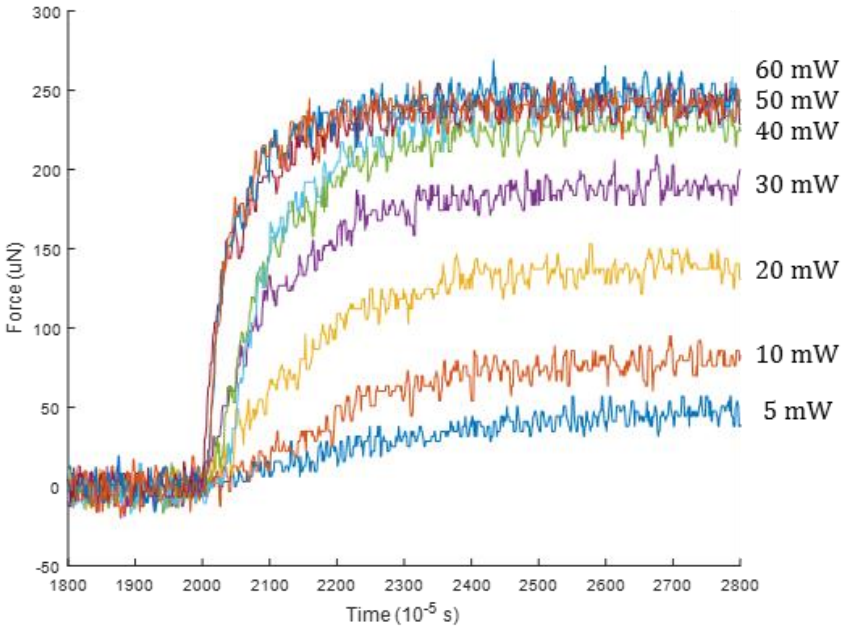

Figure 59 Saturation of response speed in the laser irradiation condition over 40 mW

Through these data, we can set the optimum laser condition for actuation to 50 mW, which has the maximum force and highest speed. The response speed and maximum actuation force will be lower under this condition and the structure might incur damage under conditions higher than this (Figure 60).

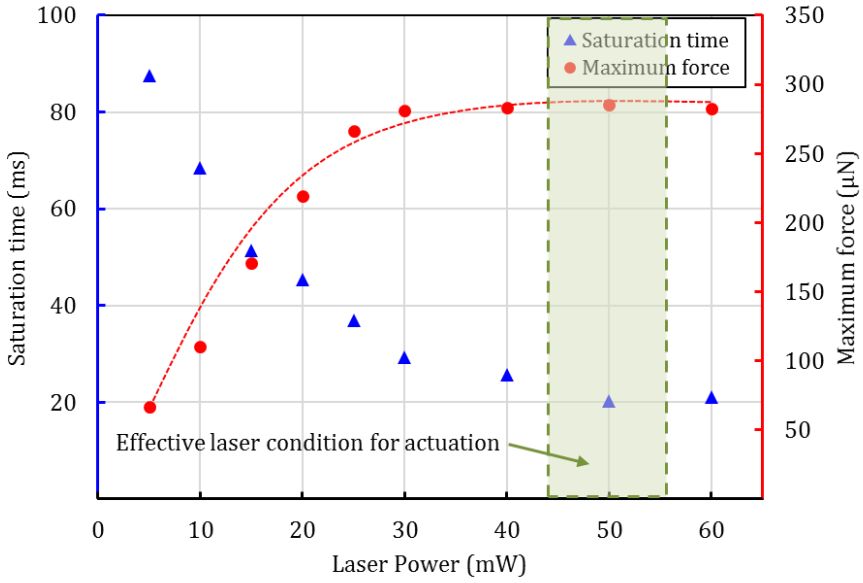

Figure 60 Graph of saturation time and maximum forces according to laser irradiation power

Additionally, similar to ion beam-induced heating, the reaction according to the on/off status of the laser was evaluated. The graphs in Figure 61 show the reaction force changes measured with various laser shutter speeds. Between 1 to 10 Hz of switching speed, the force response follows closely, with a small degree of offset at the bottom layer. When the laser switching speed increases above 50 Hz, however, the range of the reaction force change becomes smaller as the bottom line of the reaction force increases. As the laser switching speed becomes faster, there is insufficient time to cool down the structure and it does not reach the base

line. Although the force difference between peak and valley of the fluctuation of the reaction forces became smaller, the SMA structure followed laser switching until 300 Hz with reaction force changes (Figure 62).

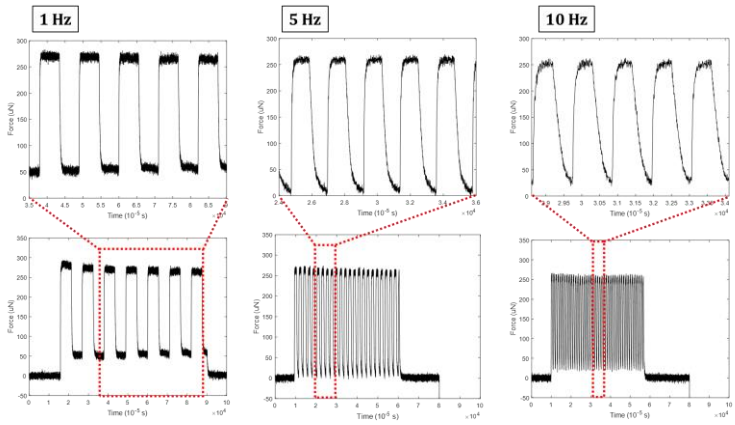

Figure 61 Response curve under switching frequency between 1 – 10 Hz

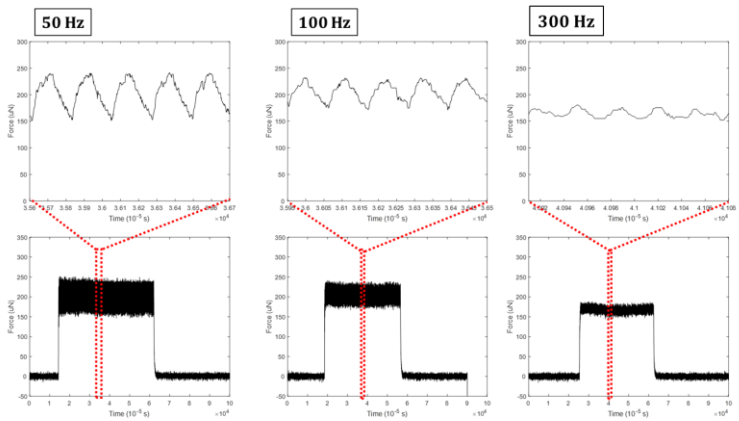

Figure 62 Response curve under switching frequency between 50 to 300 Hz

The case with switching speeds exceeding 300 Hz is shown in Figure 63. We can obtain some information regarding actuation from the phase transition of the SMA actuator, but it does not present clear fluctuation wave form due to noise in the data.

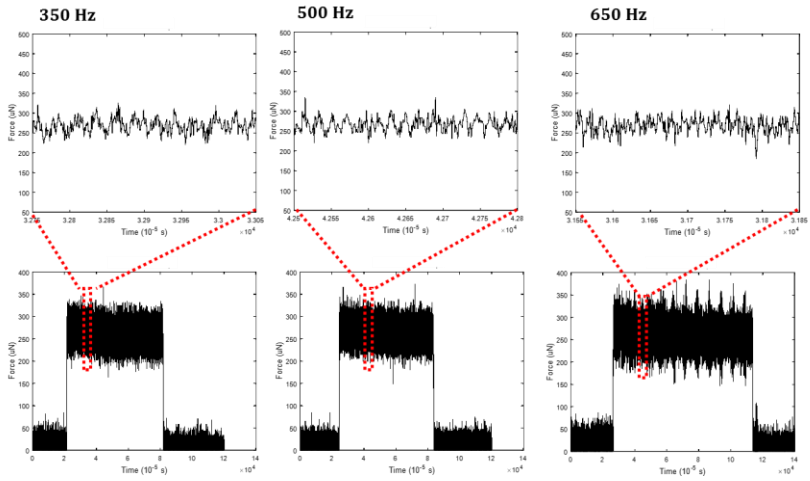

Figure 63 Response curve under high speed switching frequency between 350 – 650 Hz

To investigate responses to high-speed laser-induced SMA actuation, fast Fourier transform (FFT) analysis was performed. As shown in the graphs in Figure 64, the high peaks were measured at the same speed between driving speed of laser irradiation system for actuation and the FFT analysis results. Thus, we can conclude that the SMA actuator fabricated in this research can achieve 650 Hz of actuation speed from the laser-induced heating method.

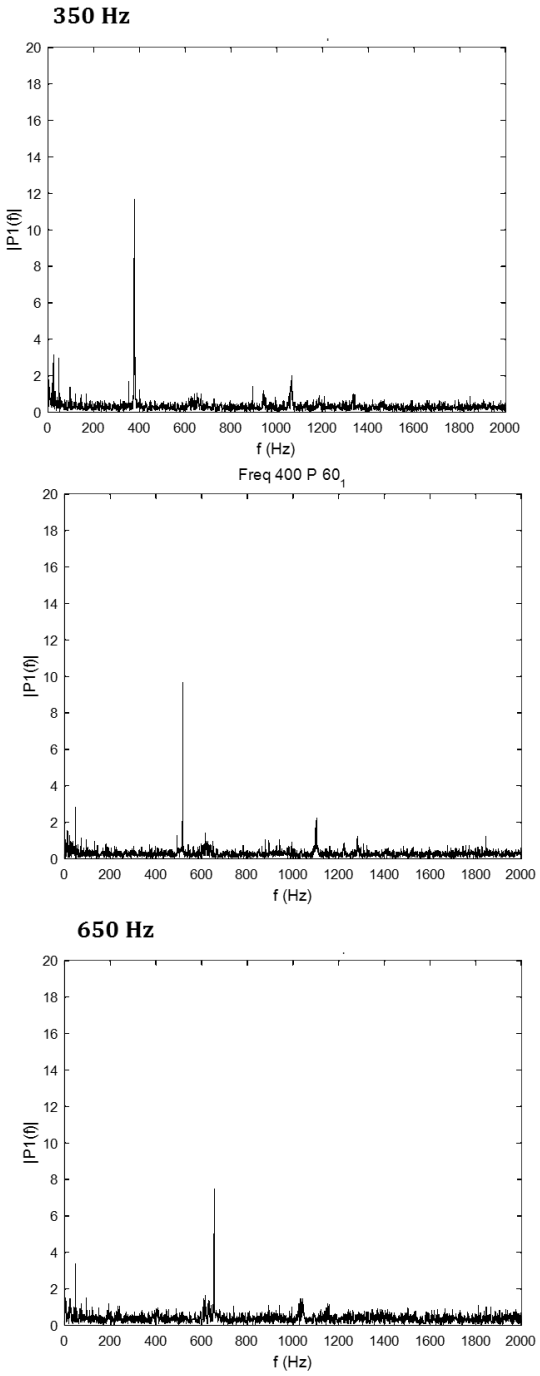

Figure 64 TTF analysis result of 350, 500, 650 Hz of switching speed of SMA actuation

The change in reaction force according to frequency is shown in Figure 65. As mentioned previously, the reaction force decreased as the frequency increased and the actuation amplitude was reduced by half between 10 and 50 Hz. The actuation amplitude decreased as the laser power increased, but the actuation force does not disappear even at an actuation speed of l,500 Hz.

Figure 65 shows the dependence of the change in reaction force on the frequency of the focused laser irradiation. The graph shows that the reaction force decreased as frequency increased, and the actuation amplitude was reduced by half at 60 Hz, corresponding to a response time of ~17 ms. The actuation amplitude increased as the laser power increased, and actuation continued even at 500 Hz, at which point pulsed heating becomes faster than heating by laser irradiation and heat dissipation through convection to ambient air. This process is slower than that of piezoelectrically driven actuators (> tens of kHz) but much faster than that of conventional shape memory alloy actuation.

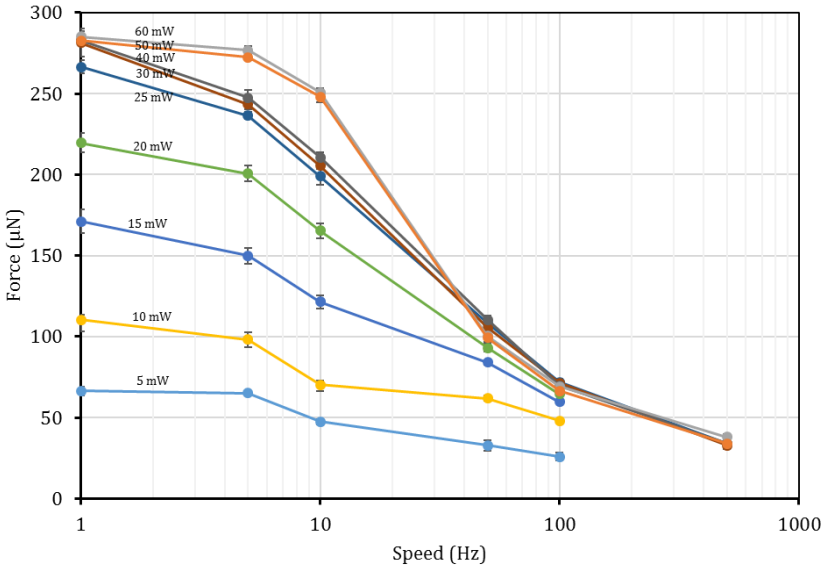

Figure 65 Graph of reaction force change in terms of laser power and actuation frequency.

5.2. Design and fabrication of Micro Gripper

As an application of ion beam-induced actuation, a prototype for a reversible microscale gripper was fabricated. Figure 66 shows the prototype of the microscale gripper. As the fabricated cell has an auxetic structure, the inner area increases as the structure is stretched, so that we can put a target material in the inner area of the cell and then grip it.

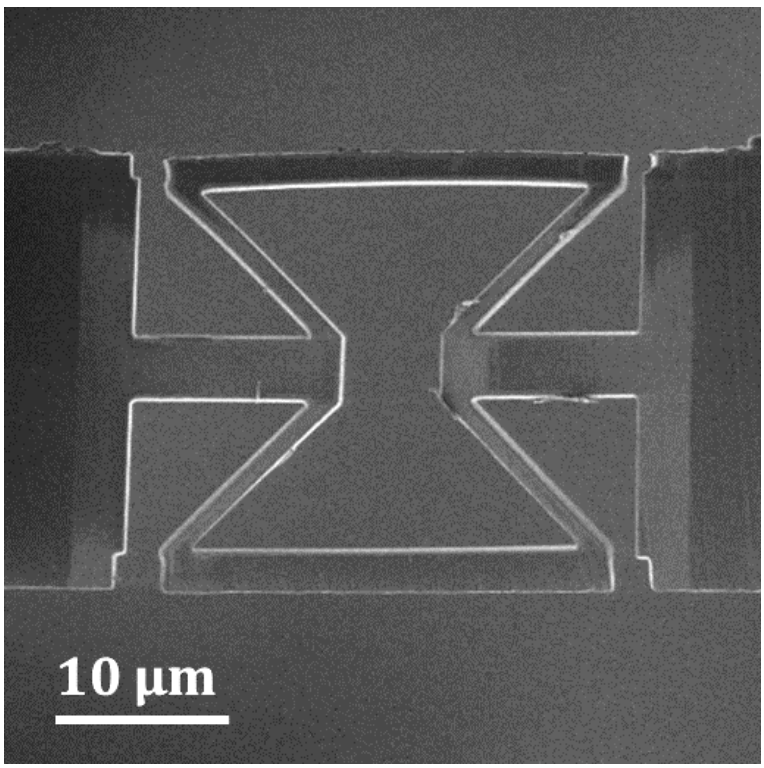

Figure 66 SEM image of a prototype of microscale gripper

Figure 67 shows the schematic process for gripper actuation. Through the stretching, release, and shape recovery steps, we can grip the object. As can be seen in the displacement-force diagram shown in Figure 68, the length of the opening can be controlled by increasing the deformation length and we can confirm that the gripper can be used repeatedly.

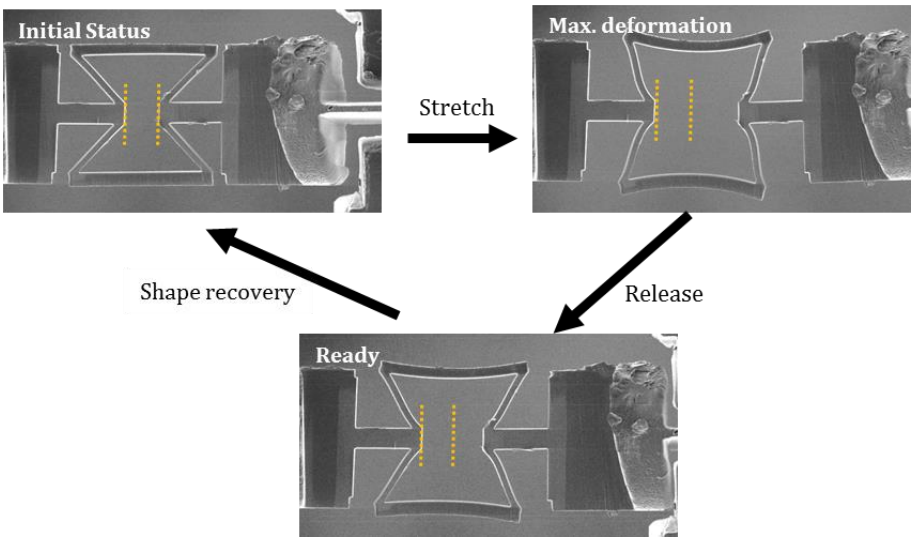

Figure 67 Actuation procedure of developed micro-gripper

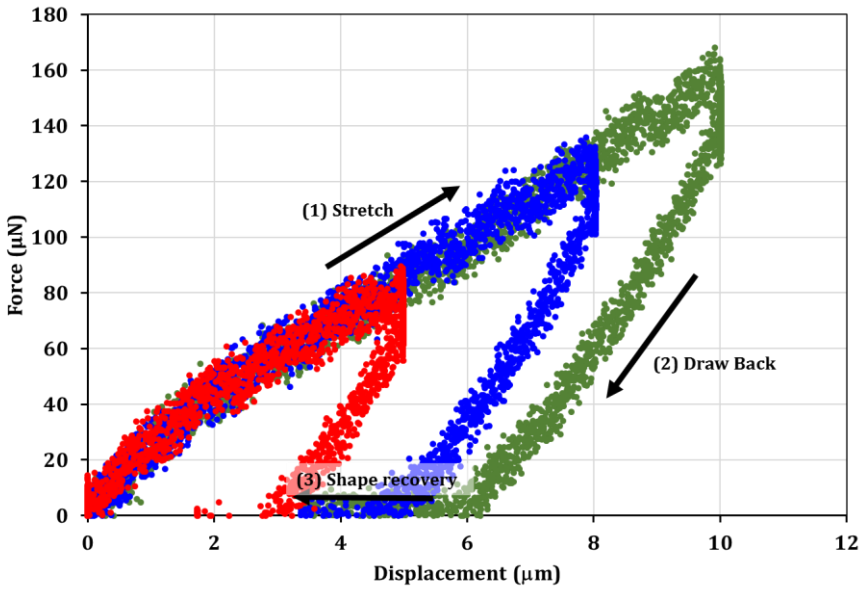

Figure 68 Diagram for gripping length and reaction force of the microscale SMA gripper

As a performance test, a microscale tungsten wire was captured using the developed prototype. First, move the gripper to the target and locate the center of the gripping area. Second, insert the target in the middle of the gripper. Third, activate the shape memory effect by heating the entire structure to grab the target. As shown in the inset pictures, after the gripping motion is completed, the target material is fixed tightly. The structure does not miss grabbed objects even under a shaking motion.

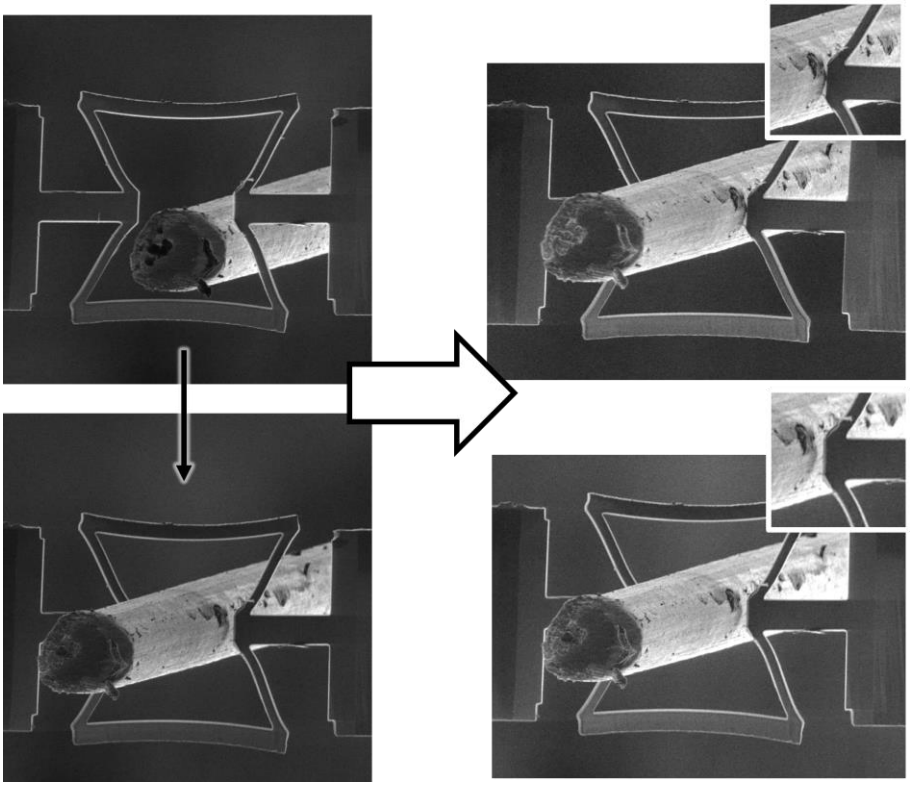

Figure 69 Demonstration for capturing micro wire by using developed micro gripper

5.3. High-speed linear vibration actuator

As mentioned in the Introduction, due to limitations in fabrication methods, it has only been possible to achieve a bending motion in the manufacture of a microscale actuator with SMA. However, in this study, because the developed SMA actuator has a spring-like shape and diamond structure, it is possible to achieve a linear motion. As a prototype, a simple linear actuator consisting of two microscale linear actuators was fabricated (Fig. 70).

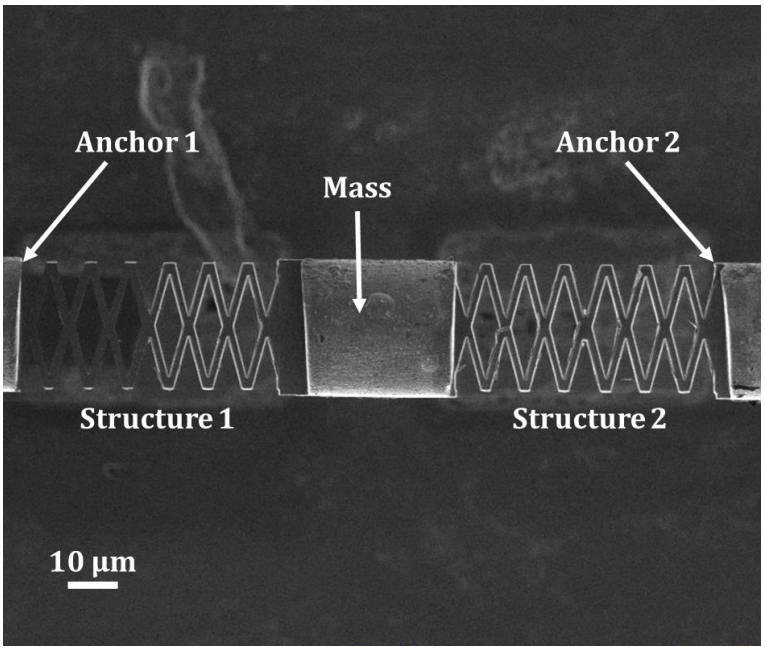

Figure 70 SEM image of SMA based micro linear actuator fabricated by FIB milling process

Figure 71 shows a schematic diagram and picture of the developed laser system used to evaluate actuation. As shown in the figure, locating a mass at the center, two diamond-shaped frame structures were placed. Because the developed SMA actuator has a spring-like shape, it can achieve linear motion even when stretched, as giving laser energy to the two parts alternatively, the mass located at the center was shaken to the left and right repeatedly due to the shape memory effect. Figure 72 shows optical microscopic images taken during the actuation test; it can be seen that the mass attached to the middle of the gripper was shaken to the left and right according to laser irradiation.

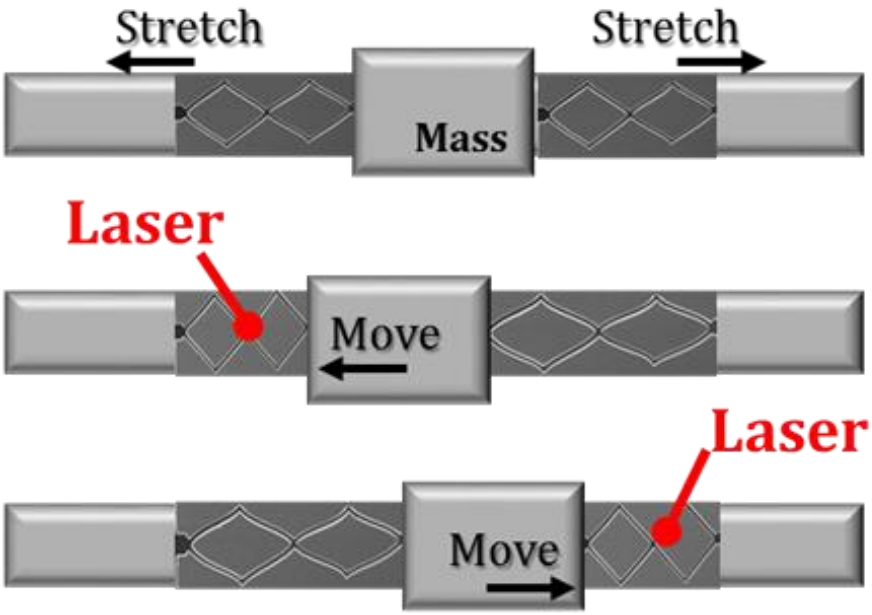

Figure 71 Schematic of microscale high speed linear actuator

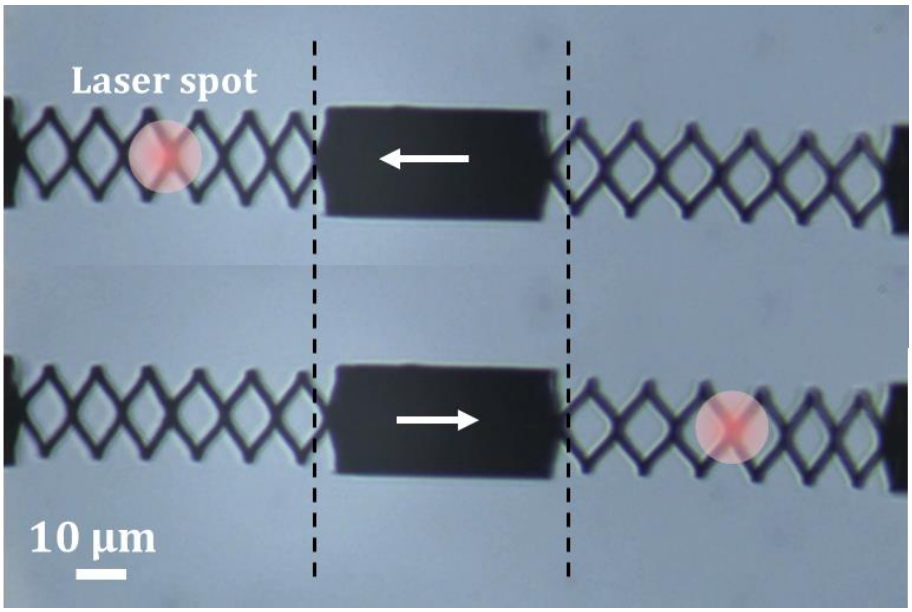

Figure 72 Images of Actuation of Microscale high-speed linear actuator taken under an optical microscope.

5.4. Actuation with 2-way shape memory effect

By repeating the stretching, release, and heating processes, the SMA structure remembers shapes at both high and low temperatures. This phenomenon is known as the two-way shape memory effect [69]. Using this, we can produce a free-standing actuator (Fig. 73). Although actuation with the two-way shape memory effect has a slower actuation speed than one-way actuation and does not provide as much force, it is useful for developing microscale robots because it can actuate without any bias forces. The picture shown in Figure 74 is an image captured during the actuation motion of a two-way linear actuator. This actuator can move repeatedly with no bias forces.

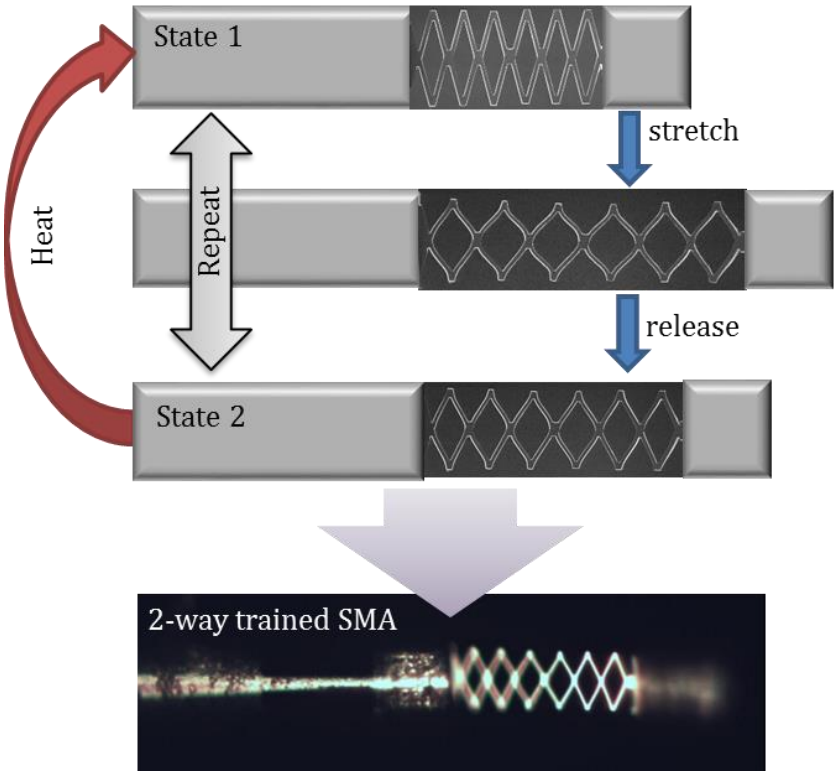

Figure 73 Schematic of microscale two-way actuation

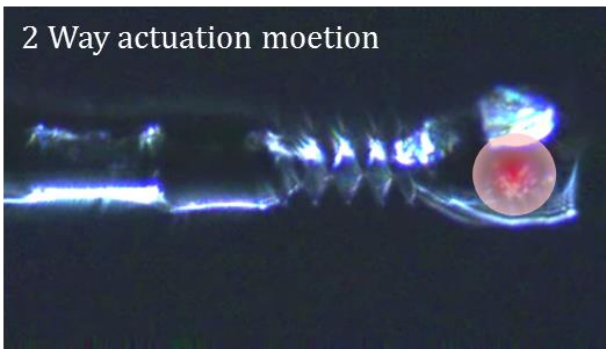

Figure 74 Optical microscopic image of actuation with two-way motion

Chapter 6. Conclusions

In this study, it is aimed to design, fabricate and evaluate of shape memory alloy based microscale actuator and robot. To achieve complex shape fabrication and in-situ characterization process, a sample manipulation and characterization platform equipping high-resolution nanopositioners with a multi degree of freedom, micro-force sensor, and micro-gripper. The challenge in precise and accurate fabrication for the samples with complex geometry was overcome and this platform can be used for mechanical property characterization with the in-situ method in the high vacuum chamber of focused ion beam (FIB) system.

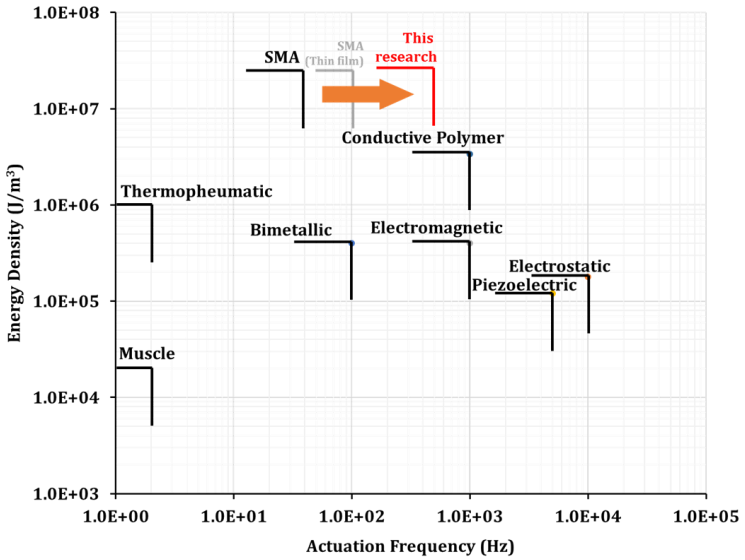

Figure 75 Comparison of micro-actuation mechanism and result in this research

With aid of this proposed platform, 2-dimensional frame structure arrays having 1.5 μm thickness were manufactured by focused ion beam (FIB) milling process. In addition, the behavior of these structures under mechanical deformation or thermal condition change were investigated to utilize SMA structure as driving force for the microscale actuator or robot.

As an application, microscale swimming robot was proposed. Microscale linear motion actuator can vibrate with 500 Hz of actuation speed and a gripper at the tail grab and deliver an objective. We can expect that the proposed actuators can contribute to developing micro-/nanoscale devices for microscale investigation or medical purposes.

Bibliography

1. Martel, S., et al., *Automatic navigation of an untethered device in the artery of a living animal using a conventional clinical magnetic resonance imaging system.* Applied Physics Letters, 2007. **90**(11): p. 114105.

2. Solovev, A.A., et al., *Catalytic microtubular jet engines self-propelled by accumulated gas bubbles.* Small, 2009. **5**(14): p. 1688-92.

3. Zhang, L., et al., *Characterizing the swimming properties of artificial bacterial flagella.* Nano letters, 2009. **9**(10): p. 3663-3667.

4. Ghosh, A. and P. Fischer, *Controlled propulsion of artificial magnetic nanostructured propellers.* Nano letters, 2009. **9**(6): p. 2243-2245.

5. Magdanz, V., S. Sanchez, and O.G. Schmidt, *Development of a Sperm-Flagella Driven Micro-Bio-Robot.* Advanced Materials, 2013. **25**(45): p. 6581-6588.

6. Búzás, A., et al., *Light sailboats: Laser driven autonomous microrobots.* Applied Physics Letters, 2012. **101**(4): p. 041111.

7. Hu, W., K.S. Ishii, and A.T. Ohta, *Micro-assembly using optically controlled bubble microrobots.* Applied Physics Letters, 2011. **99**(9): p. 094103.

8. Pawashe, C., S. Floyd, and M. Sitti, *Modeling and Experimental Characterization of an Untethered Magnetic Micro-Robot.* The International Journal of Robotics Research, 2009. **28**(8): p. 1077-1094.

9. Pawashe, C., S. Floyd, and M. Sitti, *Multiple magnetic microrobot control using electrostatic anchoring.* Applied Physics Letters, 2009. **94**(16): p. 164108.

10. Kummer, M.P., et al., *OctoMag: An Electromagnetic System for 5-DOF Wireless Micromanipulation.* IEEE Transactions on Robotics, 2010. **26**(6): p. 1006-1017.

11. Zhou, Y., S. Regnier, and M. Sitti, *Rotating Magnetic Miniature Swimming Robots With Multiple Flexible Flagella.* IEEE Transactions on Robotics, 2014. **30**(1): p. 3-13.

12. Sul, O.J., et al., *Thermally actuated untethered impact-driven locomotive microdevices.* Applied Physics Letters, 2006. **89**(20): p. 203512.

13. Diller, E. and M. Sitti, *Three-Dimensional Programmable Assembly by Untethered Magnetic Robotic Micro-Grippers.* Advanced Functional Materials, 2014. **24**(28): p. 4397-4404.

14. Miyashita, S., E. Diller, and M. Sitti, *Two-dimensional magnetic micro-module reconfigurations based on inter-modular interactions.* The International Journal of Robotics Research, 2013. **32**(5): p. 591-613.

15. Tasoglu, S., et al., *Untethered micro-robotic coding of three-dimensional material composition.* Nat Commun, 2014. **5**: p. 3124.

16. Donald, B.R., et al., *An Untethered, Electrostatic, Globally Controllable MEMS Micro-Robot.* Journal of Microelectromechanical Systems, 2006. **15**(1): p. 1-15.

17. Martel, S. and M. Mohammadi. *Using a swarm of self-propelled natural microrobots in the form of flagellated bacteria to perform complex micro-assembly tasks*. in *Robotics and Automation (ICRA), 2010 IEEE International Conference on*. 2010. IEEE.

18. Fearing, R.S., et al. *Wing transmission for a micromechanical flying insect*. in *Robotics and Automation, 2000. Proceedings. ICRA'00. IEEE*

International Conference on. 2000. IEEE.

19. Choudhary, N. and D. Kaur, *Shape memory alloy thin films and heterostructures for MEMS applications: A review.* Sensors and Actuators A: Physical, 2016. **242**: p. 162-181.

20. Mohd Jani, J., et al., *A review of shape memory alloy research, applications and opportunities.* Materials & Design (1980-2015), 2014. **56**: p. 1078-1113.

21. Committee, A.H., *Metals Handbook: Vol. 2, Properties and selection–nonferrous alloys and pure metals.* American Society for Metals, Metals Park, OH, 1978.

22. Hodgson, D.E., W. Ming, and R.J. Biermann, *Shape memory alloys.* ASM International, Metals Handbook, Tenth Edition., 1990. **2**: p. 897-902.

23. Otsuka, K. and X. Ren, *Physical metallurgy of Ti–Ni-based shape memory alloys.* Progress in Materials Science, 2005. **50**(5): p. 511-678.

24. Clark, B.G., et al., *Size Independent Shape Memory Behavior of Nickel-Titanium.* Advanced Engineering Materials, 2010. **12**(8): p. 808-815.

25. San Juan, J., M.L. Nó, and C.A. Schuh, *Thermomechanical behavior at the nanoscale and size effects in shape memory alloys.* Journal of Materials Research, 2011. **26**(19): p. 2461-2469.

26. Kim, C.-S., S.-H. Ahn, and D.-Y. Jang, *Review: Developments in micro/nanoscale fabrication by focused ion beams.* Vacuum, 2012. **86**(8): p. 1014-1035.

27. Picard, Y.N., et al., *Focused ion beam-shaped microtools for ultra-*

precision machining of cylindrical components. Precision Engineering, 2003. **27**(1): p. 59-69.

28. Igaki, J.-y., et al., *Three-dimensional rotor fabrication by focused-ion-beam chemical-vapor-deposition.* Microelectronic Engineering, 2006. **83**(4-9): p. 1221-1224.

29. Antoniou, N., K. Rykaczewski, and M.D. Uchic, *In situ FIB-SEM characterization and manipulation methods.* MRS Bulletin, 2014. **39**(04): p. 347-352.

30. Gianola, D.S., et al., *In situ nanomechanical testing in focused ion beam and scanning electron microscopes.* Review of Scientific Instruments, 2011. **82**(6): p. 063901.

31. Wheeler, R., et al., *In-situ mechanical testing of micro-sized specimens fabricated by FIB.* Microscopy and Microanalysis, 2008. **14**(S2): p. 100-101.

32. Allison, P.G., et al., *In-situ nanomechanical studies of deformation and damage mechanisms in nanocomposites monitored using scanning electron microscopy.* Materials Letters, 2014. **131**: p. 313-316.

33. Gianola, D. and C. Eberl, *Micro-and nanoscale tensile testing of materials.* JOM, 2009. **61**(3): p. 24-35.

34. Legros, M., D. Gianola, and C. Motz, *Quantitative in situ mechanical testing in electron microscopes.* MRS bulletin, 2010. **35**(05): p. 354-360.

35. Noyong, M., et al., *In situ nanomanipulation system for electrical measurements in SEM.* Measurement Science and Technology, 2007. **18**(12): p. N84.

36. Pantano, M.F., H.D. Espinosa, and L. Pagnotta, *Mechanical characterization of materials at small length scales.* Journal of Mechanical Science and technology, 2012. **26**(2): p. 545-561.

37. Kihara, Y., et al., *Tensile behavior of micro-sized specimen fabricated from nanocrystalline nickel film.* Microelectronic Engineering, 2015. **141**: p. 17-20.

38. Calahorra, Y., et al., *Young's modulus, residual stress, and crystal orientation of doubly clamped silicon nanowire beams.* Nano letters, 2015. **15**(5): p. 2945-2950.

39. Bechtle, S., et al., *A method to determine site-specific, anisotropic fracture toughness in biological materials.* Scripta Materialia, 2012. **66**(8): p. 515-518.

40. Chan, Y., A. Ngan, and N. King, *Use of focused ion beam milling for investigating the mechanical properties of biological tissues: a study of human primary molars.* Journal of the mechanical behavior of biomedical materials, 2009. **2**(4): p. 375-383.

41. Utke, I., S. Moshkalev, and P. Russell, *Nanofabrication using focused ion and electron beams: principles and applications*. 2012: Oxford University Press.

42. Adineh, V.R., et al., *Multidimensional characterisation of biomechanical structures by combining Atomic Force Microscopy and Focused Ion Beam: A study of the rat whisker.* Acta biomaterialia, 2015. **21**: p. 132-141.

43. Biallas, G. and H.J. Maier, *In-situ fatigue in an environmental scanning electron microscope–Potential and current limitations.* International journal of fatigue, 2007. **29**(8): p. 1413-1425.

44. Orso, S., et al., *Micrometer-Scale Tensile Testing of Biological*

Attachment Devices. Advanced Materials, 2006. **18**(7): p. 874-877.

45. Shi, C., et al., *Recent advances in nanorobotic manipulation inside scanning electron microscopes.* Microsystems & Nanoengineering, 2016. **2**: p. 16024.

46. Bilegt, E., et al., *Design and evaluation of micro-cutting tools for local planarization.* International Journal of Precision Engineering and Manufacturing, 2016. **17**(10): p. 1267-1273.

47. Hadley, N.F., *The arthropod cuticle.* Scientific American, 1986. **255**: p. 104-112.

48. Peter, M., G. Kegel, and R. Keller, *Structural studies on sclerotized insect cuticle*, in *Chitin in nature and technology*. 1986, Springer. p. 21-28.

49. Minelli, A., G. Boxshall, and G. Fusco, *Arthropod Biology and Evolution: Molecules, Development, Morphology*. 2013: Springer Science & Business Media.

50. Yilmaz, E.D., H. Jelitto, and G.A. Schneider, *Uniaxial compressive behavior of micro-pillars of dental enamel characterized in multiple directions.* Acta biomaterialia, 2015. **16**: p. 187-195.

51. Kiener, D., et al., *FIB damage of Cu and possible consequences for miniaturized mechanical tests.* Materials Science and Engineering: A, 2007. **459**(1): p. 262-272.

52. Kato, N., Y. Kohno, and H. Saka, *Side-wall damage in a transmission electron microscopy specimen of crystalline Si prepared by focused ion beam etching.* Journal of Vacuum Science & Technology A, 1999. **17**(4): p. 1201-1204.

53. Barber, D.J., *Radiation damage in ion-milled specimens:*

characteristics, effects and methods of damage limitation. Ultramicroscopy, 1993. **52**(1): p. 101-125.

54. Narayan, K. and S. Subramaniam, *Focused ion beams in biology.* Nature methods, 2015. **12**(11): p. 1021-1031.

55. Hazekamp, J., et al., *Focussed ion beam milling at grazing incidence angles.* Journal of microscopy, 2011. **242**(1): p. 104-110.

56. Liu, B., et al., *In situ probing the interior of single bacterial cells at nanometer scale.* Nanotechnology, 2014. **25**(41): p. 415101.

57. Hepburn, H. and A. Ball, *On the structure and mechanical properties of beetle shells.* Journal of Materials Science, 1973. **8**(5): p. 618-623.

58. Lee, H.-T., et al., *Site-specific characterization of beetle horn shell with micromechanical bending test in focused ion beam system.* Acta Biomaterialia, 2017.

59. Kato, N.I., *Reducing focused ion beam damage to transmission electron microscopy samples.* Journal of electron microscopy, 2004. **53**(5): p. 451-458.

60. Mayer, J., et al., *TEM Sample Preparation and FIB-Induced Damage.* MRS Bulletin, 2011. **32**(05): p. 400-407.

61. Mikmeková, Š., et al., *FIB induced damage examined with the low energy SEM.* Materials Transactions, 2011. **52**(3): p. 292-296.

62. Fu, J., S.B. Joshi, and J.M. Catchmark, *A study of angular effects in focused ion beam milling of water ice.* Journal of Micromechanics and Microengineering, 2008. **18**(9): p. 095010.

63. Howell, L.L., *Compliant mechanisms*. 2001: John Wiley & Sons.

64. Howell, L.L., S.P. Magleby, and B.M. Olsen, *Handbook of compliant*

mechanisms. 2013: John Wiley & Sons.

65. Divringi, K. and C. Ozcan, *Advanced Shape Memory Alloy Material Models for ANSYS.* Ozen Engineering Inc, 2009.

66. Frick, C.P., et al., *Orientation-independent pseudoelasticity in small-scale NiTi compression pillars.* Scripta Materialia, 2008. **59**(1): p. 7-10.

67. Ishitani, T. and H. Kaga, *Calculation of local temperature rise in focused-ion-beam sample preparation.* Journal of Electron Microscopy, 1995. **44**(5): p. 331-336.

68. Patra, N., et al., *Parametric investigations on the influence of nano-second Nd 3+ :YAG laser wavelength and fluence in synthesizing NiTi nano-particles using liquid assisted laser ablation technique.* Applied Surface Science, 2016. **366**: p. 104-111.

69. Duerig, T.W., K. Melton, and D. Stöckel, *Engineering aspects of shape memory alloys*. 2013: Butterworth-Heinemann.

70. Lantada, A.D., A. Muslija, and J.P. García-Ruíz, *Auxetic tissue engineering scaffolds with nanometric features and resonances in the megahertz range.* Smart Materials and Structures, 2015. **24**(5): p. 055013.

요약 (국문초록)

형상기억 합금을 이용한 마이크로스케일 고속 구동기의 제작 및 평가

이 현 택

서울대학교 기계항공공학부기계전공 대학원

본 연구에서는 집속이온빔 가공 공정을 이용하여 고속 구동이 가능한 형상기억합금 기반의 마이크로스케일 구동기를 제작하였다. 집속이온빔 밀링 공정을 이용하여, 두께 1 마이크로미터의 골격으로 이루어진 마름모 형태의 마이크로스케일 고속 구동기를 제작하였다. 집속이온빔 내에서 제작 시편의 조작 및 복잡한 형상 제작이 가능하도록 진공 환경에서 운용 가능한 나노스케일의 분해능을 가진 시편 이송장치 및 마이크로스케일 집게와 힘센서 등으로 이루어진 집속이온빔 내 실시간 시편조작 및 물성측정 장치를 구축하였다. 구축된 장치를 이용하여, 다양한 형태의

형상기억합금 구조물을 제작하였으며, 형상 변형에 따른 구조물의 반발력 측정 및 형상기억 효과 확인과 같은 물성 측정 과정을 시편의 이송 없이 진행하였다.

제작된 구조는 마이크로스케일에서 얻을 수 있는 크기효과를 통하여 빠른 속도의 온도 변화와 그에 따른 상변화 효과를 얻을 수 있어, 500 Hz 수준의 고속 구동이 가능하다. 또한 마름모 형태의 구조는 길이 방향의 인장시의 구조 변화를 통하여 4-8% 수준의 재료 변형한계를 능가하는 변형 및 복원이 가능하며, 마름모 각도의 구조 변화를 통하여 인장력 및 인장 길이의 조절이 가능하다.

구조물 구동은 이온빔 또는 레이저 조사 방식과 같은 광학적 방식을 통하여 에너지를 조사하는 방식으로 구동하게 되며, 이 방식은 전류 및 기타 제어를 위한 와이어링이 필요하지 않고, 형상기억 효과에 의한 구동방식을 사용하여, 간단한 방식으로 구동이 가능한 특징을 가지고 있다.

주요어 : 형상기억합금, 마이크로스케일, 구동기, 집속이온빔

학 번 : 2011-23340